Materials Horizons

Organic chiral nano- and microfilaments: types, formation, and template applications

Journal:	*Materials Horizons*
Manuscript ID	MH-REV-08-2023-001390.R1
Article Type:	Review Article
Date Submitted by the Author:	22-Oct-2023
Complete List of Authors:	Gowda Muniyappa, Ashwathanarayana; Kent State University, Advanced Materials and Liquid Crystal Institute Pathak, Suraj; Kent State University, Advanced Materials and Liquid Crystal Institute Rohaley, Grace; Kent State University, Materials Science Graduate Program, Advanced Materials and Liquid Crystal Institute Acherjee, Gourab; Kent State University, Department of Chemistry and Biochemistry and Advanced Materials and Liquid Crystal Institute Oprandi, Andrea; Kent State University, Materials Science Graduate Program, Advanced Materials and Liquid Crystal Institute Williams, Ryan; Kent State University, Materials Science Graduate Program, Advanced Materials and Liquid Crystal Institute Prévôt, Marianne; Kent State University, AMLCI Hegmann, Torsten; Kent State University, Advanced Materials and Liquid Crystal Institute

Impact Statement

Organic chiral nano- and microfilaments: types, formation, and template applications

Chiral thread-like structures are pervasive in nature at virtually all length scales, from amyloid fibrils associated with brain disorders the meter-long narwhal tusks. With the chiral shape imparting unique functions, chiral filamentous objects are part of our daily lives, from screws and springs to staircases and buildings.

Recognizing the tunable nature of chiral filaments, research over the last years has focused on functional materials that allow for the generation of chiral filaments varying in size, shape, helical pitch, and ability to serve as template.

Effective design of chiral filaments toward applications in medicine, sensing, metamaterials, as well as optical, catalytic, and electronic applications requires a deep understanding of the mechanisms responsible for filament formation and evolution. Introducing a unifying concept of intra- and interlayer misfits, this review uses examples from classes of materials forming chiral filaments to explain how the various filament shapes form and why, and how they are used as templates for nanoscale and luminescent materials. By using simple geometric considerations as the basis for our discussion, we trust that the study and utility of chiral nano- and microfilaments will continue to excite materials research and seek more complex and applicable chiral filaments solutions to pressing societal problems.

{word count = 200}

REVIEW

Organic chiral nano- and microfilaments: types, formation, and template applications†

Received 00th August 2023,
Accepted 00th January 20xx

DOI: 10.1039/x0xx00000x

Ashwathanarayana Gowda,[a] Suraj Kumar Pathak,[a] Grace A. R. Rohaley,[a,b] Gourab Acharjee,[c] Andrea Oprandi,[a,b] Ryan Williams,[a,b] Marianne E. Prévôt,[a-c] and Torsten Hegmann*[a-d]

Organic chiral nanofilaments are part of an important class of nanoscale chiral materials that has recently been receiving significant attention largely due to their potential use in applications such as optics, photonics, metameterials, and potentially a range of medical as well as sensing applications. This review will focus on key examples of the formation of such nano- and micro-filaments based on carbon nanofibers, polymers, synthetic oligo- and polypeptides, self-assembled organic molecules, and one prominent class of liquid crystals. The most critical aspects discussed here are the underlying driving forces for chiral filament formation, potentially answering why specific sizes and shapes are formed, what molecular design strategies are working equally well or rather differently among these materials classes, and what uses and applications are driving research in this fascinating field of materials science.

1. Introduction

Chiral filamentous structures are omnipresent building blocks in nature, found equally in flora and fauna at length scales ranging from a few nanometer in one, two, or all three dimensions all the way to multi-meter-long macroscopic objects. Prominently, chiral filaments at small scales include nucleic acids (DNA, RNA) and nanoscale filaments formed by proteins, peptides, and enzymes[1] such as tau amyloid fibrils,[2, 3] crenactin[4] and tubulin[5, 6] helical structures found in various single cell organisms as well as bacteria[7] and helical virus nucleocapsids[8] among others. On the larger scale, helical filament structures are seen in narwhal tusks,[9] animal horns,[10] plant tendrils,[11] and seed pods[12] to name a few. Frequently mimicked in form and function by synthetic or engineered objects for reasons ranging from pure aesthetics and functionality to enhanced directional stability or flexibility, chiral filaments are also part of our macroscopic day-to-day life. Springs, many types of corkscrew worms (bladed worm, speed worm, Auger worm, and several others), pasta, 3-D printed helical polymers,[13] Archimedes' screws, and an ever-increasing number of twisted high-rise buildings[14] are just some examples. In materials science, chiral filaments with nanoscale dimensions are increasingly generated and studied for promising uses in optics, photonics, sensing, and many other applications. While researchers' attention focuses equally on inorganic[15-17] as well as organic building blocks to generate chiral nanofilaments, this review will focus exclusively on organic chiral nanofilaments. By discussing a select number of example systems, the aim is to (1) draw analogies in nanofilament formation among the most prevalent materials classes, (2) work out and compare common design principles, and (3) elucidate the underlying driving forces for chiral nanofilament formation. Finally, we will conclude with some exemplary applications, especially drawing from the more recent work where such chiral nano- and microfilaments serve as chiral templates for other materials.

2. Chiral organic nano- and microfilament shapes

2.1. Types of filaments and some theoretical considerations

Before we begin discussing specific organic materials known to form chiral nano- and perhaps also larger microfilaments, we should begin looking in more detail into the distinct types of chiral filament shapes and shape variations.

Filaments can be composed of either a single rod-shaped or flat ribbon shaped subfilament or of multiple individual ones either stacking on top of or twisting around one another. The cross-sections of the resulting filaments are then most commonly flat, elliptical, or round. Solid rod- or tube-like subfilaments with a round cross-section can assemble into single, double, or multi-twisted cylindrical or twisted tape-like fibers with the average orientation of the rod-like fibers parallel to or at an angle with respect to the helical axis. An example of a 90° angle here would be the chiral nematic (or cholesteric) phase formed by rod-like molecules,[18] nanorods,[19] or rod-like viruses.[20]

Flat ribbons, however, can form single or multilayer helicoids, screw helices, or helical ribbon structures (cylindrical helices). In these twisted along or continuously bent around extremes, helicoids are essentially twisted helices with Gaussian saddle-like curvature featuring a straight centerline, while cylindrical as well as screw helices are characterized by cylindrical curvature and a helical centerline; with the flat ribbon either bent around

---

[a] Advanced Materials and Liquid Crystal Institute, Kent State University, Kent (OH) 44242 USA
[b] Materials Science Graduate Program, Kent State University, Kent (OH) 44242 USA.
[c] Department of Chemistry and Biochemistry, Kent State University, Kent (OH) 44242 USA
[d] Brain Health Research Institute, Kent State University, Kent (OH) 44242 USA.

† Electronic Supporting information (ESI) accompany this article.

Figure 1. Possible ways to transform a flat ribbon to chiral ribbons; t and w are the height and width of the ribbon filament, respectively; d is the diameter when the cross-section changes from rectangular to circular (i.e., from a ribbon to a cylinder or tube). The filament angle θ, assuming two sub-layers with orthogonal anisotropic properties (e.g., expansion, shrinkage, or packing – adopted from refs. 12 and 22), mathematically referred to as 'misfits', as well as w and t determine the type of chiral filament ultimately formed. Continuous bent around t along a helical center line leads to screw helices, continuous bent around w along a helical centerline to cylindrical helices, and twist along a straight centerline to helicoids (twisted ribbons). When $w = t = d$, continuous bent around d along a helical centerline generates common helices (single-, double-, or multi-). For multilayer chiral ribbons, as highlighted in the examples discussed, the type of chiral filament sets the limits for the number of layer stacks (t) and filament width (w). (P)- and (M)- are the helicity.

the width (w) or bent around the height (i.e., the thickness, t) as schematically shown in Figure 1.

Work by Sharon *et al.*, studying the geometry and mechanics of seedpod opening, showed that two dimensionless parameters determine the ensuing chiral shape.[12, 21] The first is the angle θ between the ribbon long axis and directions of curvature (i.e., the fiber directions), the second is the dimensionless width $\tilde{w} = w(\kappa_0/t)^{1/2}$, where w, t, and κ_0 are the width, thickness, and intrinsic curvature of the ribbon respectively.[12, 22] In analogy to bilayers, where two sublayers orthogonally shrink or expand unidirectionally thereby inducing curvature, θ, t, and w, as indicated in Figure 1 (center and top left corner),[22] become the essential parameters governing type, pitch, and handedness (one handedness for values of θ between 0° and 90° and the opposite handedness for values between 90° and 180°). For example, for single flat as well as multilayer flat ribbons, θ, t, and w determine which shape is favorably formed with Sharon et al.'s work[12] and Dumais et al.'s analysis[22] already indicating that the formation of helicoids requires $\theta \sim 45°$ and that larger w favor the formation of cylindrical but not screw helices. Self-limiting w and t accompanying the formation of stacked twisted helicoidal ribbons (twisted sublayer stacks) were theoretically described by Grason.[23-25] Fundamentally, helicoids formed by sublayer stacks can only be stable for limited w and t, and w and t are closely correlated, thus leading to a finite number of layer stacks. Monte Carlo simulations of the interaction parameter space governing experimentally observed crossovers between Gaussian saddle-like and cylindrical curvature, notable changes in helical pitch length, even handedness inversion have been presented by Selinger and coworkers among others.[26]

Mathematical models of layer stacks can calculate that so-called 'misfits' (forms of anisotropic multi-layer configuration) cause rod- or ribbon-like filaments to twist or form helices.[27] Often, the exact nature of misfits, which are highlighted throughout this review, are changes in chirality, some pronounced biaxial symmetry of the constituent molecular aggregates or building blocks, differences in layer shrinkage or expansion direction (like the opening of seedpods[12]) as well as lattice strain among several others that determine whether a flat ribbon twists, writhes, or perhaps even both.[28]

In the following sections we will discuss five specific classes of organic synthetic materials for which chiral nanofilaments have frequently been described. These include purely carbon-based materials (often referred to as helical carbon fibers or HCFs), synthetic oligo- and polypeptides, supramolecular assemblies formed by small molecules, polymers, and finally a specific class of bent-core liquid crystals (Figure 2a). Wherever possible, we highlight and explain the differences or similarities in chiral filament formation and how the underlying concept of 'misfits' leads to twisting or writhing. These include template effects, packing frustration, amphiphilicity, intrinsic chirality, molecular conformations leading to supramolecular chirality, and chiral additives (Figure 2b) that can be tailored to generate those observed but also other desirable chiral nanofilament types, all

Figure 2. **(a)** Types of materials known to form organic chiral nanofilaments that are reviewed and compared. **(b)** Overview of the influencing factors leading to 'misfits' that ultimately result in twisting (writhing) while also serving as parameters that affect pitch, overall dimensions, shape, and 3-D packing of organic nanofilaments.

with a final focus on applications in optics, photonics, or simply the use as a template for another type of material.

There are, of course, other examples of materials classes that do not fall within these five categories. As we can use them to demonstrate some of the concepts, we want to discuss them at least briefly. Among some of the most prominent examples are bilayer helicoidal, flat, or helical filaments formed by certain Gemini surfactants (where two identical surfactant molecules are covalently joined by a short aliphatic hydrocarbon spacer).[29] In the presence of chiral counterions (depending, among other factors, on the enantiomeric excess, *ee*) that permit hydrogen bonding between adjacent chiral counterions in the bilayer structure such as ethylene-1,2-bis(dimethylalkylammonium) D- or L-tartrates (e.g., 16-2-16 D- or L-tartrate), these surfactants show rich polymorphism.[30] The resulting bilayer filaments can further serve as templates after ion exchange and silicification with a silane precursor such as TEOS (Figure 3a).[31] The critical choice of the right type of chiral counterion was demonstrated using chiral malate ions (lacking one of the hydroxy groups), where weakened hydrogen bonding interactions between opposite counterions resulted in the formation of flat but not twisted or helical ribbons.[29]

To illustrate how morphology and dimensions of the helices and helicoids can be tuned, studies on using temperature changes and introducing small amounts of achiral additives (i.e., achiral counterions such as bromide) highlighted that flat ribbons as well as helicoids and cylindrical helices with varying pitch are accessible and quite easily interconvertible (Figure 3b).[30] Given progressive shape transformations and the fact that tubules formed by cylindrical helices ultimately prevail, modulations of the tilt direction of individual molecules with respect to their neighbors was postulated to first give rise to ripples within the ribbons when twisted ribbons transform to helical ribbons, as suggested theoretically.[26] These then lead to domain walls. The ensuing cylindrical helical ribbons display characteristic stripes, which finally coalesce to form tubular structures with a helical wrapping.[30]

In addition, a whole range of other lipid bilayers, as reviewed by Fuhrhop and Helfrich,[32] can form a plethora of cylindrical or twisted helices that are often unstable (since the formation of helical fiber morphologies in these systems is a kinetically controlled process[30]), ultimately serving as precursors for helical tubules, where the ribbon edges make contact (see decreasing pitch, p, for cylindrical helices in Figure 1), just as in the case of Gemini surfactants. Aside from external factors such as temperature or rate of temperature change, the molecular structure of the surfactant or amphiphile largely determines the filament morphology outcome, and racemates usually lead to morphology that do not express chirality, i.e., they tend to form flat ribbons. Thus, when properly combined, these two factors generate the necessary misfits for helical filament formation.

Another intriguing class of materials with demonstrated rich filament polymorphism are some types of viruses with rod- and spindle-like shapes (e.g., fd virus[20, 33, 34] or spindle-like archaeal viruses like bicaudavirus SMV1[35]). Aqueous suspensions of fd virus with noninteracting polymers, after several hours of phase separation, show the formation of helicoidal ribbons about 1 µm in width (i.e., equal to the length of the fd virus) out of striped tactoids with the director perpendicular to the helix axis as in the chiral nematic phase (top DIC images in Figure 3c).[36] Near equilibrium, these fd virus assemblies form flat 2D membranes, which, under certain conditions, transition at the edges to 1D twisted ribbons due to negative line tension.[20]

However, in this review we will focus mainly on more synthetic materials, and for ease of use, we will use smaller, simplified versions of the pinwheel diagrams for both the type of material and origin of engineered 'misfits' shown in Figure 2 throughout this review.

2.2. Chiral carbon nano- and microfilaments

Without knowing the exact makeup of the so-called "vermicular threads," Davis and coworkers first reported the discovery of chiral or helical carbon fibers (HCFs) in 1953,[37] almost 40 years prior to the monumental disclosure of the formation of carbon nanotubes (CNTs) by Ijima.[38] HCF formation was likely the result of interactions between carbon monoxide and iron oxide in so-

Figure 3. (a) Chemical structure of 16-2-16 L-tartrate; (i) TEM image after 24 h aging (right-handed cylindrical helices) and (ii) after ion exchange with Br^- ions and silicification using tetraethyl orthosilicate (TEOS). The related 16-2-16 L-malate forms flat ribbons. TEM images reprinted with permission from ref. 31, Copyright 2016 Royal Society of Chemistry. **(b)** (i) – (iii) TEM images showing the evolution of morphologies of 16-2-16 L-tartrate after (i) 2 h, (ii) 3 h, and (iii) after 36 h. (iv) – (vii) TEM images demonstrating the effect of adding 16-2-16 $2Br^-$ to the morphologies of ribbons formed by 16-2-16 L-tartrate with *ee* ~ 1: (iv & v) 1% 16-2-16 $2Br^-$, where initially formed twisted ribbons transformed into helical ribbons and then into tubules after several days, (vi) 1.5% 16-2-16 $2Br^-$, where only twisted ribbons were observed, and (vii) where flat ribbons were formed after the addition of 4.7% 16-2-16 $2Br^-$; (viii & ix) plot and schematic of the variation of the pitch as a function of the *ee* of L-tartrate. Reprinted with permission from ref. 30, Copyright 2007 American Chemical Society. **(c)** (top) Schematic representation of the filamentous fd virus (px with x = 3, and 6-9) are proteins around the two central antiparallel ssDNAs. Reprinted with permission from ref. 34, Copyright 2017 Royal Society of Chemistry. Examples of digital interference contrast (DIC) micrographs of single layer smectics forming helices on the surface of either metastable nematic drops (set of top images, reprinted with permission from ref. 36, Copyright 2001 Royal Society) or showing a polymorphic transition from flat 2D membranes to helicoidal ribbons. Scale bars = 5 µm. Reprinted with permission from ref. 33, Copyright 2005 Elsevier.

called iron-spots within the brick (where extreme temperatures of the firing process along with exposure to oxygen cause the iron to flare). Even initial attempts to describe the mechanism were spot on, considering that the authors noted that particles of an iron-based catalyst (iron or iron carbide) were residing in the growing ends of the carbon-based helical threads.[37]

Over the last three decades, however, the discoveries of CNTs, fullerenes, and graphene have continuously fueled the search for other carbon-based materials and morphologies.[39] Synthesis methods reported largely follow some form of nanoparticle-assisted growth (by combustion chemical vapor deposition, CCVD).[40-42] Considering the twisted or helical nature of the HCF products, we deduce that the origin of curvature is related to the curvature of fullerenes.[43-45] Insertion of pentagonal rings into graphene sheets leads to positive curvature while insertion of heptagonal and/or octagonal rings to negative curvature—a combination of which introduces a bend (or 'knee') into the polygonal graphene sheet.[45] Absence of knees leads to tubular structures (e.g., multi-walled CNTs) or morphologically achiral fibers of stacked graphene sheets.[46] The knee notion caused by pentagon/heptagon pairs, as well as distortions within hexagon graphene fragments[47] (as misfits), are considered the principal mechanisms behind for the formation of toroidal or helical

Figure 4. (a) Side and top views of HCNTs: penta- at inner and heptagon rings at outward ridges. **(b)** Structural evolution under tension loading. Reprinted with permission from ref. 48, Copyright 2013 American Chemical Society.

Figure 5. (a) (i) SEM image of HCFs about 100 nm in width prepared by decomposition of acetylene catalyzed by copper nanoparticles. TEM images in (ii) – (vi) show the facetted Cu nanocrystals embedded in the HCNFs – nanocrystal shape and orientation determine the HCFs overall shape and handedness always serving as the origin for two HCF filaments. Reprinted with permission from ref. 54, Copyright 2004 Elsevier. **(b)** (i) – (iv) Helical carbon nanofibers (HCNF) generated by acetylene decomposition in the presence of iron/iron carbide (Fe/Fe_3C) nanocrystals – composition and particle size again affect critical parameters of the HCNF growth. Reprinted with permission from ref. 53, Copyright 2010 American Chemical Society. **(c)** TEM images of HCNFs generated by electrolysis in molten electrolytes consisting of Li_2CO_3 and Li_2O with 1% Fe_2O_3 with double-helix morphology (as shown the inset (braided helices) and **(d)** shows SEM images when a higher concentration of Fe_2O_3 was used (i.e., 1.7% Fe_2O_3) – the morphology changes to a bladed worm helical corkscrew. Reprinted with permission from ref. 55, Copyright 2021 Elsevier. **(e)** Various double-helical carbon microfilaments created by the spinning of CNT films generated single-walled CNTs via CVD using ferrocene as a catalyst. Reprinted with permission from ref. 56, Copyright 2013 American Chemical Society. **(f)** Examples of shape and morphology variations in HCF including single and double helices, or torus. Reprinted with permission from ref. 41, Copyright 2011 Elsevier. **(g)** Twisted ribbon morphology observed for a self-assembled structure between random coil polystyrenes modified with nucleobases to generate hydrogen bonds as well as pyrene for π-π interactions with CNTs (see chemical structure at right). In the absence of chiral bias, as expected, both right- and left-handed ribbons were observed. Reprinted and adapted with permission from ref. 57, Copyright 2013 Wiley-VCH. Models at the bottom (side and top view) visualize the misfit leading in helicoidal ribbon twist for most but not all the flat lamellar filaments.

(coiled) CNTs (HCNTs, Figure 4).[48] In the formation of helical carbon nanofibers (HCNFs), the catalyst nanoparticles assist in generating these misfits. Thus, ensuing differences in interfacial tension and wettability[49] and the inherent presence of facets on polygonal particle surfaces (i.e., the particle's morphology)[50-55] are considered as the most plausible and correlated aspects to describe HCNF formation.

Some typical examples of helical carbon nanofibers (HCNFs), including various electron microscopy images of HCNFs showing the embedded catalyst nanoparticles, are collected in Figure 5a-c.[53-55] Even when the process of HCNF formation is not based on the pyrolysis of acetylene in the presence of a metal-based catalyst but using electrolysis in a molten salt containing a metal oxide such as Fe_2O_3 (Figure 5c), particles do appear as the site from where HCNFs begin growing.[55] Shape, concentration (i.e., the weight fraction of), and composition among several other nanoparticle parameters largely affect dimension, morphology, and handedness of the ensuing HCNFs (Figure 5d).

More complex helical and double-helical architectures were generated by the spinning of single-walled CNT films. Starting with an initially straight CNT yarn, a combination of overtwisting and/or applying an external force at the yarn's midpoint were shown to generate both symmetrical as well as asymmetrical double-helical CNT yarn morphologies (Figure 5e).[56]

Considering that CNTs with a spherical cross-section were the starting point, it is perhaps not surprising that most HCNFs form single-, double- or more complex hierarchical helical filaments. More elusive morphologies include tori, cylindrical helices, and figure-8 loops among others (Figure 5f). However, an example of helicoidal fibers was also realized by using single-walled CNTs in combination with achiral random or block copolymers.[57] The helicoidal twisted ribbons formed here due to a combination of well-designed intermolecular forces between the CNTs and the co-polymers (such as π-π interactions or stacking between a pyrene-functionalized short tether with the CNTs as well as by hydrogen bonding between introduced nucleobases; Figure 5g). A survey of the provided TEM images in this work offered clues as to what is to be expected, i.e., that the absence of a chiral bias in the system led to the formation of both left- and right-handed helicoidal filaments. The misfit here originates from the underlying long-range ordered lamellar structure formed by the composites, as deduced from small angle X-ray scattering data, and the ensuing steric bulk imparted by close-packed polymer chains at the lamellae peripheries, ultimately leading to twist.

2.3. Chiral polymer nano- and microfilaments

While steric demand imparted by polymer building blocks led to twisted CNT ribbons in the last example, we will now focus on some representative examples demonstrating the formation of chiral nano-, micro-, even macrofilaments based on synthetic polymers.

There are countless examples of helical polymers[58] of biological origin or with significant technological relevance such as DNA (and synthetic DNA mimics[59]), collagen[60], polyisocyanates[61-63], or poly(phenylacetylene)s[64]. However, we purposefully choose to limit the discussion to examples with morphologically chiral filament architectures and expressly highlight causes for their formation. A typical example of such a superhelical structure is shown in Figure 6a. Depending on the composition and the solvent used, poly(γ-benzyl-L-glutamate)-block-poly(ethylene glycol) (PBLG-*b*-PEG) and homo-poly(γ-benzyl-L-glutamate) (homo-PBLG) can cooperatively assemble into hybrid helical nanofilaments or helical ring-like architectures in water.[65]

In a solvent mixture of THF/DMF, the experimentally observed packing mode is that of a rigid rod homopolymer and a rod-coil block-co-polymer. Water, when added, selectively swells only

Figure 6. (a) Model showing the formation of helical filament assemblies by mixtures of block-co-polymers and homopolymers (here: poly(γ-benzyl-L-glutamate)-block-poly(ethylene glycol) (PBLG-*b*-PEG) in H_2O and homo-poly(γ-benzyl-L-glutamate) (homo-PBLG)); the PBLG blocks form the core and the PEG blocks the cladding. SEM image shows filaments with ~ 140 nm width and ~80 nm pitch. Reprinted with permission from ref. 65, Copyright 2009 Royal Society of Chemistry. **(b)** Tri-fluid electrospinning of hollow helical and grooved helical nanofilaments: (i) off-centered spinneret leading to grooved (top) and concentric spinneret resulting in coaxial hollow helical nanofilaments after immersion in water, (ii) SEM image of single helical nanofilament with grooved structure as a biomimetic example for a coiled tendril of loofah vine (upper-right insert shows a withered grooved loofah tendril after drying – grooves highlighted by red arrows). Reprinted with permission from ref. 67, Copyright 2021 Elsevier. **(c)** Morphology-composition diagram obtained from self-consistent field theory calculations for ABC terpolymer micelles in a selective solvent; f_A, f_B, and f_C are the relative lengths of the A, B, and C blocks, respectively. Structures with helical cores are largely reserved for select compositions (HHS = spheres with two helix cores) but also exist as superhelices at the transition between RRC (cylinders with two ring-like cores) and DDC (super-cylinders with two disc-like cores). Reprinted with permission from ref. 68, Copyright 2011 Royal Society of Chemistry. **(d)** (i) Macroscopic helical ribbons from helical polymer fibers formed by polyaniline (PANI) doped with (*S*)- or (*R*)-camphor sulfonic acid (CSA). (ii) Flat ribbons forming in THF are transitioning to cylindrical helical ribbons with a decrease in the helical pitch after introducing and increasing to proportion of *iso*-propanol as predicted by theory and further confirmed by *g*-factor and ellipticity data, and (iii) helical 'self-motion' introduced by the addition of a chiral amine (both enantiomers). Scale bars: 0.5 mm. Reprinted with permission from ref. 69, Copyright 2018 Springer Nature. **(e)** Self-assembly of chiral polyesters into exclusively left-handed helical filament superstructures in a 1:1 CH_2Cl_2/n-hexane solvent mixture. Reprinted with permission from ref. 75, Copyright 2019 American Chemical Society. **(f)** Helical polyacetylene (H-PA) structures formed via chiral nematic liquid crystal templating: (i) concept and corresponding SEM images and (ii) demonstration of the hierarchical assembly. Reprinted with permission from ref. 79, Copyright 2020 Wiley-VCH.

the PEG block, and the ensuing increase in interfacial tension between the PBLG and the PEG block is only relieved by twisting into a helix, similar to the example described earlier of seedpods opening.[21] While inherently chiral, PBLG, somewhat depending on its molecular weight and processing conditions, typically forms straight nanofibers or simple rods composed of densely packed PBLG helix bundles.[66] Thus, packing frustration between polymer blocks caused by a differential swelling in a selective solvent is the misfit that leads to twist.

Related hollow or grooved core-shell nanofilaments can also be generated by tri-fluid electrospinning with the final morphology controlled by the spinneret type.[67] Combining a thermoplastic polyurethane as outer fluid (blue in Figure 6b) with cellulose acetate as middle fluid (pink) and polyvinylpyrrolidone (PVP) as inner fluid (green) leads to grooved core-shell helical filaments when an off-center spinneret is used to hollow core-shell helical filaments using a concentric spinneret as soon as the inner PVP component is washed out with either water or ethanol. Helical structure formation is the result of engineered mismatches between the mechanical properties (misfit) of the components during stretching in the electric field—even with handedness inversions as seen for plant tendrils such as by Towel Gourd.[11]

Further insights into such ternary multicore polymer systems were uncovered by self-consistent field calculations. The model inspected the solution-state multicore micelle self-assembly of linear ABC terpolymers consisting of a solvophilic mid-block and two mutually incompatible solvophobic end-blocks. The final observed structural regions for these multiblock micelles are shown in the plot in Figure 6c. In addition to a sphere containing two helix cores (HHS), the calculations also revealed a so-called superhelix at the transition between RRC (cylinder with two ring-like cores) and DDC (supercylinder with two disc-like cores), which is best described as a double helix of two incompatible blocks, as shown in Figure 1 (top right), in the continuum of the third.[68]

The roles that solvent compatibility and microstructure played in these experimental and theoretical examples can further be upscaled to virtually macroscopic and tunable helical filaments, as revealed by the example shown in Figure 6d.[69]

While induction of chirality in polyaniline (PANI) by enantiomers of camphor sulfonic acid ((*R*)-CSA and (*S*)-CSA) as chiral dopants has been studied at the molecular, nano-, and micro-scale,[70-74] this concept has recently been validated at the macro-scale as well. Initial sub-mm ribbons were prepared by self-assembly on uniaxial stretched polypropylene substrates and subsequently peeled down in THF. In THF, the macroscale ribbons are quasi flat. However, adding iso-propanol and steadily increasing the proportion of this protic solvent transforms the flat ribbons into cylindrical helices and eventually into tubular structures as seen for the decreasing pitch of cylindrical helices given in Figure 1. The configuration of CSA here dictates the handedness of the helical filaments. Given that iso-propanol is a poorer solvent for PANI than THF, increasingly diluting THF with iso-propanol induces some degree of intermolecular shrinkage (or shrinkage strain) difference within the ribbon – the outside vs. the inside thereby generating the misfit that leads to cylindrical curvature, again in analogy to the seedpod opening described earlier. Given the larger width of the ribbons, cylindrical curvature to mitigate the strain was expected. The ensuing morphological difference between the outside and the inside of these ribbons was even visible in AFM images. Noteworthy further, is the versatility of such filaments for chiral sensing. Exposure to either enantiomer of a chiral amine, as shown in sub-panel (iii) (Figure 6d) first leads to a visible color change and then to an enantiomer-specific twisting motion to a final twisted ribbon-based hollow tubule.[69]

Just as the handedness of the cylindrical helices was decided by the configuration of the dopant's chiral center in the previous example, chiral centers deliberately introduced in the backbone of polyesters can furnish polymer nanofilaments with a specific handedness (Figure 6e).[75] Remarkably, however, both (*S*)-poly-3 as well as (*R*)-poly-3 (independent of whether the R group was heptyl or phenyl) formed exclusively left-handed helical filaments after precipitation in CH_2Cl_2/n-hexane. Moreover, the acryloyl group (explicitly the C＝C bond) turned out to be a prerequisite for the formation of helical filaments. Once reduced, the helicity as well as any sort of fiber morphology vanished and some quasi-spherical colloidal particles of ~ 50 nm in diameter were formed instead. The authors thus assumed that the side chains (at the chiral centers) in combination with a stiffer backbone provided by the unsaturated C＝C bond are only contributing to steric demands affecting the packing of polymer chains (that we assume to be the misfit), somehow in analogy to conformational effects observed for chiral side chains in helical poly(phenylacetylene)s.[76, 77] Such effects are decidedly reliant on the nature and polarity of the solvent, surely meriting similar studies in such unsaturated polyesters using more polar (protic and aprotic) solvents.

If, however, isotropic solvents are traded for chiral liquid crystal solvents, polymeric filamentous structures with a helical sense can be prepared in a chiral reaction field (Figure 6f).[78-82] Here, a low molecular weight nematic liquid crystal (N-LC) was first doped with a potent chiral additive generating a chiral nematic LC (N*-LC) phase with either a left- or right-handed tunable pitch. In the given case, these system parameters were adjusted by changing the temperature. Precisely, temperature changes drive changes in the helicity, i.e., changes in the conformation determined by the dihedral angle between the linked naphthyl rings[83, 84] but not changes in configuration of the axially chiral binaphthyl-based chiral dopant.[79] Using this dynamic medium then as a solvent for the polymerization of acetylene led to either left- or right-handed films with multi-hierarchical chiral morphologies (panel (ii) in Figure 6f).

Overall, just as was the case for the carbon-based nanofibers, polymer nano- and microfilaments tend to predominantly form cylindrical helices of flat ribbons or filament helices with circular cross-sections. Given the narrow constraints set by the filament angle θ and width w ($\theta \sim 45$ ° and narrow width, see Figure 1) for an intralayer misfit, the lack of observed helicoids is thus not surprising.

2.4. Oligo- and polypeptide-based chiral nano- and microfilaments

Closely related to polymers, oligo- and polypeptides are another fascinating class of materials able to form morphologically chiral nano- and microfilaments.[85] Recurrently, motifs structurally (chemically) related to those forming amyloid fibrils, involved in amyloid-associated brain disorders (i.e., neurodegenerative diseases) such as Alzheimer's or Parkinson's disease,[86, 87] are at the core of many of these investigations.[3] Commonly, however, tubular structures formed by cylindrical helices are the most thermodynamically stable morphological configurations, even if other morphologies are formed first.

Figure 7. (a) (i) Chemical structure of CapFF heptapeptide modified from the amyloid-β (16-20) fragment (KLVFF core motif), (ii) depiction of all intermediate and final polymorphic steps observed with time, and (iii) related AFM images of twisted ribbons (left), helical ribbons (middle), and final cylindric helical nanotube (right) – all left-handed. Reprinted with permission from ref. 88, Copyright 2011 Wiley-VCH. **(b)** Chemical structure of the C_{16}-KKFFVLK peptide amphiphile and illustration of the thermos-reversible morphological transition between twisted ribbon and cylindrical helix and tubule; (ii) – (iv) Cryo-TEM images showing the various nanoscale morphologies: (ii) coexisting nanotubules and cylindrical helices, (iii) single nanotubule, and (iv) twisted ribbons (helicoids); (v) birefringent texture observed by polarized optical microscopy (POM). Reprinted with permission from ref. 90, Copyright 2013 Royal Society of Chemistry. **(c)** (i) Chemical structure and simplified model of the peptide amphiphile $C_{16}H_{31}O$-VEVEGRGD and (ii) TEM images showing the evolution of twisted nanoribbons from larger wider flat ribbons depending on the concentration in aqueous solution. Reprinted with permission from ref. 91, Copyright 2009 American Chemical Society. **(d)** (i) Chemical structure of oligopeptide amphiphiles KI_3FK (no —OH group), KI_3YK (*para* —OH group), and KI_3DopaK (*para* & *meta* —OH group), (ii) TEM images of the morphological evolution with time from helicoids to cylindrical helical tubules, and (iii) proposed hydrogen-bonding model for adjacent fibers. Reprinted with permission from ref. 93, Copyright 2021 Elsevier. **(e)** (top) Schematic illustration showing the helical assembly driven by the chiral interactions between the ferrocene-$^{\mathrm{L}}$Phe-$^{\mathrm{L}}$Phe-OH dipeptide and a chiral diamine (here (*R*)- and (*S*)-1-methylpiperazine); the molecular structures were obtained from the single-crystal X-ray structure analysis. (i) – (ix) Illustration and side-view SEM images showing the morphological evolution of the hierarchical helical arrays (HHA) with increasing time after water vapor annealing. Reprinted with permission from ref. 94, Copyright 2021 American Chemical Society. **(f)** (i) Chemical structure of the S30L12 polypeptide and (ii) graphic showing the morphological evolution and transition depending on the solvent used. (iii) TEM images of S30L12 morphologies developing over time in 10% acetonitrile in H_2O. Reprinted with permission from ref. 95, Copyright 2020 American Chemical Society.

An example where all the polymorphic intermediates were seen is depicted in Figure 7a.[88] After an onset of isotropic-like micelle formation, the heptapeptide CapFF in aqueous solution forms structures that signify the transitions, initially over hours and finally days, from distinct protofilaments over flat to cylindrical ribbons, and ultimately to tubular structures where the filament edges join. As a kinetically controlled process, various elements appear to be involved that ultimately result in the misfits for the various intermediate shapes. At the protofilament level, self-assembly into a liquid crystalline (nematic) state seems critical. Short-range attractions (perhaps Lenard-Jones) between them lead to aggregation into the ribbon like filaments, and finally electrostatic repulsion (as the intralayer misfit) leads to twist.[89] Any energetic penalty from exposed edges is ultimately reduced by the formation of tubular structures.

Such morphological transitions can be thermally reversible as shown for a heptapeptide amphiphile (C_{16}-KKFFVLK, Figure 7b). As expected for a kinetically controlled process, cylindrical helices and tubular structures co-existed at low temperature (T = 22 °C), while at higher temperature (T = 55 °C) twisted flat ribbons (helicoids) were detected.[90]

In stark contrast to the usual observation of kinetically stable tubular structures formed by cylindrical helices, giant flat and even grooved flat nanoribbons were reported for another C_{16}-heptapeptide ($C_{16}H_{31}$OVEVE shown in Figure 7c(i)).[91] Depending on the concentration of this heptapeptide amphiphile in water, ranging from 0.01 to 0.1 wt%, helicoids varying in width and/or wide flat nanoribbons were detected. At the low concentration, helicoids dominate and at the intermediate concentration (0.05 wt%), helicoids join to form wider, flat multilayer nanoribbons (or nanobelts). These then dominate at higher concentration as seen in panel (ii); Figure 7c. Given the dimensions of w = 150 nm and t = 4.3 nm, the formation of flat multilayer nanoribbons is not at all surprising given the geometric considerations given in Figure 1 and discussed in section 2.1.[21] Ultimately, grooved nanobelts consisting of single bi- but not multi-layer ribbons are observed at higher pH values because of electrostatic repulsion between the deprotonated carboxylate groups in $C_{16}H_{31}$OVEVE, which are additionally lower in width (w = 50 vs. 150 nm).[91]

Lack or presence of hydrogen bonding was also assessed for the self-assembly of peptide bolaamphiphile variants of KI_4K (Figure 7d). Replacing phenylalanine (KI_3FK)[92] first with tyrosine (KI_3YK featuring one —OH group) followed by Dopa-lysine (KI_3FDopaK; two —OH groups).[93] While all three oligopeptides containing aromatic amino acids transitioned from helicoids to cylindrical helices to tubules over time and under now established kinetic control, —OH groups on the phenyl ring alleviated steric strain by forming polar zippers (panel (iii) in Figure 7d) between the β-sheets that ultimately led to an increase in nanotubule diameter in the order KI_3FK, KI_3YK, and KI_3DopaK.

An unusual and unexpected chiral morphology that consists of twisted multi-helical filaments featuring crystalline subfilament with a circular cross-section (amyloid-β-type nanofibrils) was reported for a diphenylalanine peptide modified with a redox-active ferrocene moiety at the N-terminus (Figure 7e)[94] after addition of a chiral amine (here 1-methylpiperazine = 1-MP). The resulting highly ordered hierarchical helical arrays (HHAs), after controlled water vapor annealing, were left-handed when (*R*)-1MP was added and right-handed in the case of (*S*)-1-MP addition. The evolution (growth) of these HHAs for the (*S*)-1-MP case is shown in panels (i) – (ix) in Figure 7e. Here again, some degree of chiral nematic ordering was assumed to be a key early step in the self-assembly process.[94]

Overall, morphological transitions in di-, oligo, and polypeptides largely follow the same trends in morphological transitions from helicoids to tubules via cylindrical helices.[1] Case in point is the recently reported self-assembly of the polypeptide S30L12 as a function of solvent composition (panels (i) and (ii) in Figure 7f).[95] S30L12 first forms curved sheets as a precursor for cylindrical helices and ultimately nanotubules at lower EtOH proportions, while twisted ribbons (helicoids) appeared as a starting point for nanotubule formation at higher EtOH proportions (panel (iii) in Figure 7f). At even higher EtOH concentrations (30% in H_2O), morphologies resembling the earlier described flat nanobelts are formed with smaller filaments emerging from them (just like those shown in panel (ii); Figure 7c; at 0.5 wt%). In acetonitrile (ACN), however, supported by solvent clustering around the filaments, helicoids are the dominating morphological species at a concentration of 30% ACN in H_2O. Amphiphilic S30L12 is comprised of hydrophilic polysarcosine, and six hydrophobic dipeptide repeat units of L-leucine and aminoisobutyric acid. Obviously, in the more polar protic solvent mixture (EtOH/H_2O) exposure of the hydrophobic moieties is better avoided by the formation of closed tubules via cylindrical helices; not necessitated in the less protic solvent mixture ACN/H_2O.

In the majority of amphiphilic oligo- and polypeptide systems, a combination of intrinsic chirality and tapered molecular shapes (changes in cross-section along the long molecular axis) are the key driving forces in the formation of ribbons that twist along a straight centerline or are bent around the ribbon width along a helical centerline. However, a tubular morphology formed by or characterized by cylindrical helical ribbons is by far the most common.

2.5. Chiral supramolecular nano- and microfilaments

In supramolecular chiral assemblies formed by small molecules, much the same driving forces lead to virtually all possible chiral filament morphologies. Extensively reviewed by Yashima et al. in 2016,[96] we will focus only on a few representative examples, published since, and particularly on some that demonstrate that helicoids are significantly more common in these systems than in any of the classes of materials we considered thus far.

Figure 8. (a) (i) Schematic showing the self-assembly of C4-MGP in H_2O, (ii) & (iii) TEM images at 4.0×10^{-4} M or 7.0×10^{-4} M. Reprinted with permission from ref. 99, Copyright 2016 Royal Society of Chemistry. **(b)** Chemical structure of NDI-L-Glu and (i) – (iii) TEM images of the formed helicoids depending on pH: (i) pH = 3, (ii): pH = 7, and (iii) pH = 9. Reprinted with permission from ref. 101, Copyright 2018 Springer Nature. **(c)** Illustration of the self-assembly of NDI-(L-Ala-TPE)$_2$ (left) and NDI-(D-Ala-TPE)$_2$ (right) in THF/H_2O = 40:60 (v/v). Reprinted with permission from ref. 102, Copyright 2018 Wiley-VCH. **(d)** Chemical structures of DD and LL disaccharides and SEM images of the two enantiomers (left and right) as well as the racemic mixture (center). All scale bars: 10 µm. Reprinted with permission from ref. 104, Copyright 2020 Wiley-VCH.

Overall, many supramolecular chiral morphologies with physical dimensions that can be imaged by electron or atomic force microscopy are formed by aromatic or polyaromatic molecules with appended chiral moieties such as chiral side chains, amino acids, or carbohydrates. Self-assembly is frequently driven by hydrogen bonding, π-π interactions, or microsegregation of incompatible molecular subunits.[97, 98] These driving forces in combination with specifically tailored molecular shapes are generally the misfits leading to twist in the ensuing assemblies.

The first example, however, serves as a logical transition from the peptide amphiphiles described in section 2.4 and shows that some concepts of chiral morphological evolution are universal. In this specific case (see Figure 8a), a pyridinium-functionalized methyl glycyrrhetate (C4-MGP) derivative first self-assembles into right-handed cylindrical helices at sub-mM concentrations in water that further transition to tubular structures with time. With the ionic pyridinium unit serving as polar headgroup and the glycyrrhetate as hydrophobic tail, the amphiphilic molecules assemble into cylindrical helical ribbons about 10 nm in width by microsegregation of hydrophilic and hydrophobic units. And just like the polypeptide S30L12 in Figure 7f, with time these structures tend to limit exposure of the hydrophobic ribbon edges to the surrounding water by transitioning to tubules.[99]

A related ionic pyridinium amphiphile connected to an achiral anthracene unit via a flexible hydrocarbon spacer then formed a conglomerate of both right- and left-handed bilayer helicoids as it should, given the absence of a chiral bias.[100]

Two examples of the formation of helicoids are given in Figures 8b and 8c. In each case, a 1,4,5,8-naphthalenetetracarboxylic diimide is first generated by reaction of the dianhydride with an amino acid, further functionalized with L-glutamate (NDI-L-Glu in Figure 8b)[101] or with tetraphenylethylene, TPE (NDI-(L- or D-Ala-TPE)$_2$ in Figure 8c)[102]. In each case, helicoids are formed due to π-π interactions between the naphthalenetetracarboxylic diimide units and interactions between the glutamate units at the periphery for NDI-L-Glu and the considerable steric demand introduced by the TPE units in NDI-(L-Ala or D-Ala-TPE)$_2$. The type of interaction between the glutamates can be tailored by changes in pH with H-bonding interactions dominating at pH = 3 and 7, and electrostatic repulsion interactions contributing at pH = 9. These specific pH-dependent interactions then decide the handedness of the ensuing twisted ribbons: left-handed at pH = 3, right-handed at pH = 9 and a racemic conglomerate of helical ribbons at neutral pH = 7.[101] In the case NDI-(L or D-Ala-TEP)$_2$, the configuration of the alanine unit decides the ribbon handedness.[102] Another example of NDI with achiral amino acid spacers and chiral deoxycholic acid end units also showed the formation of helicoids in H_2O/THF (70/30 = v/v) mixture.[103]

What was achieved by adjusting pH for NDI-L-Glu was also realized for tetrabenzyl-modified disaccharides. The DD- and LL-enantiomeric pairs here formed exclusively left- or right-handed helicoids at a concentration of 10% of hexafluoroisopropanol in water, respectively. The racemic mixture, however, rather than forming a chiral conglomerate consisting of either handedness, formed flat extended sheets with no twist at all. Microcrystal electron-diffraction (MicroED) experiments showed that the disaccharide molecules forming these ribbons possess smectic ordering (i.e., layer ordering) with C—H···π type edge-to-face aromatic interactions between phenyl rings from adjacent molecules. This smectic-like ordering was further supported by distinctive focal-conic birefringent textures (seen by polarized optical microscopy; although not liquid crystalline). MicroED further revealed twist in this supramolecular assembly, possibly due to steric reasons between neighboring benzyl units, with a handedness derived from the chirality (configuration, D- vs. L) of two glucose units (combined as the misfit), which may also provide some clues to better understand twisting mechanisms in natural polysaccharide crystals such as cellulose nanocrystals or chitin.[104]

Recalling the geometric considerations outlined in section 2.1 and Figure 1, helicoids formed by the materials shown in Figure 8b-d require specific conditions to form and would need to fulfil specific geometric parameters: limited w, limited number of layers (i.e., limited t), and an intra- or interlayer misfit along a filament angle θ of ~ 45°. For NDI-L-Glu the ribbon width ranges from w = 130 to 200 nm while t is well below this value with $t \sim$ 30 nm. Given the considerable value for w of these ribbons, one would then expect the pitch to be large, and was in fact ranging from ~ 1.4 to 2 µm (Figure 8a).[101] For NDI-(L-Ala or D-Ala-TPE)$_2$, as expected, the physical dimensions of the helicoids are almost the same as for NDI-L-Glu (Figure 8c).[102] For the DD- and LL-enantiomeric pairs, the physical dimensions of the formed helicoids further scale to values of w ranging from about 0.5 µm to several µm, of t ranging from a few hundred nm to several µm, and helical pitch values up to p = 10 µm (Figure 8d).[104]

2.6. Chiral nano- and microfilaments formed by bent-core liquid crystal molecules

The last class of materials we will discuss here, known to form a variety of chiral nano- and microfilaments, are liquid crystal (LC) molecules with a pronounced bent molecular shape. Such bent-core molecules can form an assortment of phases (some liquid crystalline, others crystalline) including the heliconical twist-bend nematic (N_{TB})[105-112] or twist-bend smectic (SmC_{TB}) phase[113] as well as layered structures of so-called dark conglomerate (DC) or sponge phases,[114, 115] a short pitched (~ 14 nm) helical ferroelectric tilted smectic phase ($SmC_SP_F^{hel}$),[116] and those we will primarily focus on in this review, so-called helical filament-type phases.[117-122] Morphological variations of the latter now include helical nano- or microfilaments with varying dimensions (width and pitch) as well as intra- or interlayer modulation,[117, 123-127] heliconical nanocrystallites,[128] and heliconical-layered nanocylinders.[129] Without delving into the details of molecular parity violations, the absence of chiral bias in the constituent molecules — the absence of molecular chirality[117] — results in the formation of equal proportions of left- and right-handed helical filament superstructures unless there is an energetic imbalance that gives rise to symmetry breaking[130] such as a chiral additive.

The helical nanofilament or HNF phase, aptly named after the discovery of its internal structure and overall morphology by Clark et al., is an astounding example of self-assembly directed by molecular conformation. These multilayer helicoids form due to an intralayer mismatch between the two molecular halves that can only be relieved by local saddle splay. This, in turn, leads to twisted filaments composed of a limited number of layer stacks usually of about 5 to 7 layers (Figure 9).[117]

The inferred intralayer mismatch here is the inherent misfit that leads to twist. The two molecular halves tilt in orthogonal directions from the layer mid-plane, which we assume as the analogue of the filament angle θ of 45° in the case of orthogonal anisotropic sublayers shown in Figure 1 (top left). This then leads to a continuous twist of the flat ribbon along a straight centerline at ~ 2°/nm forming a helicoid. As discussed throughout, the formation of such helicoids comes with several geometric restrictions such as limited w and t (i.e., limited number of stacked layers), which is experimentally observed for HNFs: $w = t \sim 40$ nm and $p \sim 200$ nm.

Where such filaments are formed by achiral molecules, HNFs form a conglomerate composed of macroscopic chiral domains with opposite handedness. Within each domain, HNFs grow, chirality preserving (i.e., left-handed in one domain and right-handed in an adjacent domain),[118] with a secondary twist among HNFs.[131] Early portrayal of this phase, historically named B4 phase, was that of a crystalline phase.[132] Solid-state MAS-NMR experiments, however, showed that the HNF phase is neither a traditional crystalline solid nor a conventional LC.[133] HNFs are characterized by crystal or hexatic in-layer ordering.[117]

Figure 9. (i) Self-assembly of the HNF phase consisting of well-defined smectic layers with in-plane crystal or hexatic order, macroscopic polarization, and tilt of the molecular planes. (ii) Visualization of the orthogonal half-molecular tilt directions on either side of the layer midplane (the resulting misfit). (iii) Formation of nanofilaments resulting from a local preference for saddle splay layer curvature. (iv) freeze-fracture-TEM (FFTEM) image of P-12-O-PIMB (*T* = 25 °C); smectic layer spacing: *d* ≈ 5 nm. (v) FFTEM image of HNFs grown from a mixture with the calamitic LC 8CB (cooled from the isotropic phase and quenched from *T* = 37 °C). (vi) FFTEM image of individual HNFs obtained by fast cooling of P-12-O-PIMB from the isotropic to *T* = 25 °C (thermally quenched from *T* = 25°C). (vii) FFTEM image of the bulk HNF phase of P9OPIMB at *T* = 25 °C: large domains of parallel, coherently twisting HNFs (quenched from *T* = 25 °C); Circled areas show coherent twist in adjacent HNFs. Scale bars: 60 nm in (iv), 400 nm in (v) and (vi), and 370 nm in (vii). Reprinted with permission from ref. 117, Copyright 2009 American Association for the Advancement of Science.

While most of the early HNF phase materials were based on the dual Schiff-base motif such as P-*n*-O-PIMB shown in Figure 9,[134] other examples lacking the Schiff-base units emerged almost twenty years later. Some featured biphenyl units in the arms (A in Scheme 1),[135] others were based on dimers with a flexible spacer consisting of an odd number of methylene groups such as the azobenzene-based dimer B in Scheme 1.[136] Noteworthy here is that A formed HNFs within and from xerogels (in solvent such as hexane).[135] Further structural modifications particularly to the central aromatic unit (by introducing a third biphenyl segment as in compound C with n = 9 – 15; Scheme 1) gave rise to another type of HNF with a pronounced inlayer modulation (both visible as striations in TEM images and deduced from X-ray scattering data), thus, a modulated HNF phase (HNF_{mod}).[123]
Introducing chiral centers at C1 in each aliphatic side chain with the same configuration ((*S*,*S*)-1 and (*R*,*R*)-1, Scheme 1) had further consequences for the resulting HNFs. First, the two compounds only formed the HNF and no other phases on both heating from the crystalline solid and cooling from the isotropic liquid phase, with transition temperatures about 60 – 70 °C lower than the related achiral compound C with an equal but non-branched aliphatic side chain of n = 8. More crucially, (*S*,*S*)- and (*R*,*R*)-1 form dual-modulated HNFs with single handedness (no conglomerate) with intra- as well as interlayer correlation (HNF_{mod2a}; here, subscript $_{mod2}$ signifies dual modulation). The dimensions (w, t, and p) of HNF_{mod} and HNF_{mod2a} morphologies remained identical to those of the original HNFs.[127] Alternating only the configuration of the two chiral centers (as in (*R*,*S*)-1 and (*S*,*R*)-1, Scheme 1), however, led to dual-modulated HNFs with considerably larger physical dimensions ($w = t =$ 100 nm; $p =$ 350 nm), so except for p, all values increased about twofold (HNF_{mod2b}; subscript b used to indicate the larger dimension). Moreover, the configuration of the chiral center in the longer *para*-side of the molecule (*para* with respect to the central biphenyl unit) appeared to control the twist sense of the single handedness HNFs formed by each of the two compounds.[124]

Significantly more unexpected was the outcome of strategically introducing only one chiral center either in the shorter *meta*- or in the longer *para*-side of these molecules. In due course, single molecule stochastic dynamics atomistic simulations showed that the position of the chiral center at this core-chain junction (at C1) in the *meta*- or the *para*-side of these asymmetric bent-shaped molecules imparted significant changes in the core-chain angle distributions as well as in the dihedral distribution functions of the first three bonds in the aliphatic side chains.[129]

When the chiral center resides in the *para*-side, such as in (*S*)-3 and (*R*)-3 (Scheme 2), a significant shift to lower bend angles is observed at the core-chain junction in comparison to the bend angle calculated for molecule (*S*)-2 (Scheme 1) where the chiral center is situated only in the *meta*-side. Furthermore, the chiral center in the *para* side chain of (*S*)- and (*R*)-3 changes the local topology of the connection of the alkoxy chain to the molecular core, subsequently leading to more opportunities for twisted conformations than when the chiral center is situated in the *meta* side chain as in compound (*S*)-2.[126] These changes in conformational distributions due to the placement of chiral centers in the *para*- or *meta*-side affect the average molecular dimensions with a lower average aspect ratio for compounds (*S*)-3 and (*R*)-3 compared to (*S*)-2.[129, 137]

As it turned out, the sum of these conformational differences governs the type of curvature of these HNF layer structures with saddle splay for the helical microfilaments formed by (*S*)-2 and (*R*)-2 (HµFs), and cylindrical curvature in the heliconical-layered nanocylinders (HLNCs) formed by (*S*)-3 and (*R*)-3.[129]

What was particularly interesting here, was that the HµF phase formed exclusively upon rapid cooling (rapid thermal quench), while an oblique columnar (Col$_{ob}$) phase was formed on slow cooling at cooling rates of 5 °C min^{-1} or less.

Studies examining the effects of altering the position, number, and configuration of chiral centers have been performed for all chiral liquid crystalline phases (effects on the magnitudes of helical pitch, spontaneous polarization, stability etc.). From a wealth of theoretical and experimental data on chiral LC phases, two general trends emerged and were reviewed by Goodby et al. and others.[138, 139] The key findings were the following: first, increasing the length of terminal aliphatic chains appended to a chiral center positioned at the core-chain juncture diminishes the effects of chirality with increasing aliphatic chain length.

Scheme 1. Chemical structures of bent-core molecules forming nano- and microfilaments, types of morphologies formed upon slow and rapid cooling, characteristic EM or AFM images showing the filament morphology and handedness, and characteristic POM textures between crossed or slight decrossed polarizers. P-n-O-PIMB: Reprinted with permission from refs. 117, 118, and 122, Copyright 2009 American Association for the Advancement of Science, 2011 American Chemical Society, and 2001 The Japan Society for Applied Physics; A: Reprinted with permission from ref. 135, Copyright 2016 Wiley-VCH; B: Reprinted with permission from refs. 136 and 143, Copyright 2014 Royal Society of Chemistry and 2019 Springer Nature; C, (*S*,*S*)-1, and (*R*,*R*)-1: Reprinted with permission from refs. 125 and 127, Copyright 2020 American Chemical Society and 2016 Wiley-VCH; (*R*,*S*)-1 and (*S*,*R*)-1: Reprinted with permission from ref. 124, Copyright 2020 Wiley-VCH; (*S*)-2: Reprinted with permission from ref. 126, Copyright 2018 Springer Nature.

Chiral centers were described as increasingly buried in the overall structure, thereby diluting the effect of the chiral center by increasing the relative volume of the aliphatic molecular substructure, especially in smectic layers (like those in HNFs). Second, and analogously, moving the chiral center away from the core-chain juncture diminishes any restraint of rotation about the chiral center, thereby effectively reducing the effects of chirality in the side chain.[138]

Scheme 2. Chemical structures of bent-core molecules forming nano- and microfilaments, types of morphologies formed upon slow and rapid cooling, characteristic EM or AFM images showing the filament morphology and handedness, and characteristic POM textures between crossed or slight decrossed polarizers. Compounds (*S*)-3 and (*R*)-3: Reprinted with permission from ref. 129, Copyright 2019 Royal Society of Chemistry; (*S*)-4, (*S*)-5, (*R*,*R*)-6, (*R*)-7, and (*R*)-8: Reprinted with permission from ref. 140, Copyright 2021 American Chemical Society; (*S*,*S*)/(*S*,*S*)-9 and 10: Reprinted with permission from ref. 141, Copyright 2023 American Chemical Society.

How much these concepts matter to HNF phase morphologies is summarized in Scheme 2. Elongation of the aliphatic side chains while retaining one chiral center each at C1 (at the core-chain juncture; see compound (*S*)-4 and (*S*)-5 in Scheme 2) only had a minor impact on the phases formed (in case of compound (*S*)-4) or on the morphologies exhibited by both compounds. The diminished effects of molecular chirality were seen most clearly for (*S*)-5, where EM images showed no clear helicoidal wrapping as previously seen for related compound (*S*)-3 with shorter aliphatic side chains. The eventually formed cylindrical layered tubules, however, consisted of fewer layers.

Considerably more impactful on the final morphology formed was relocating the chiral center to C2 along with an additional branching point by using (*R*)-2,6-dimethylheptyloxy side chains. Conformational analyses revealed that the (*S*)- and (*R*)-2-octyloxy side chains promote a markedly smaller core-chain angle with a noticeable bend at the core-chain juncture than the chiral center at C2 for the (*R*)-2,6-dimethylheptyloxy side chains, which results in an almost linear overall shape of the bent core molecular arms.

Coupled with the diminished effect of chirality, this resulted in two new morphologies on slow cooling for (*R*,*R*)-6 (Scheme 2); the coexistence of flat nanoribbons (FNRs) and occasionally twisted nanoribbons (TNRs), while upon rapid thermal quench, left- and right-handed HNF$_{\mathrm{mod2a}}$s coexisted right next to each other despite the molecular chirality of (*R*,*R*)-6.[140] The width (w) of the FNRs, consisting of up to nine layers, was particularly striking, measuring, for a few, about 100 nm but for many up to 400 nm. The formation of different polymorphs depending only on the rate of cooling from the isotopic liquid continued when the (*R*)-2,6-dimethylheptyloxy chain was introduced on only the *meta*- or *para*-side. (*R*)-7 with the chiral side chain in the shorter *meta*-side, on slow cooling formed FNRs with a width on average of w = 360 nm, while on rapid cooling, left- and right-handed HµFs coexisted with an additional Col$_r$ (*c*2*mm*) phase. Finally, in this series, (*R*)-8 exhibited the same Col$_r$ (*c*2*mm*) phase on slow cooling and shorter (only a few µm) tubular nanocylinders (NCs) on rapid cooling that lacked any indication of cylindrical helical wrapping. Xerogels of (*R*,*R*)-6 and (*R*)-7 in hexane each formed FNRs, while (*R*)-8 formed NCs.[140]

To test if one could regulate the phase or morphology by either applying an electric field or irradiating the sample with UV light, compounds (*S*,*S*)/(*S*,*S*)-9 and 10 (Scheme 2) were introduced.[141] An applied electric field has previously been used to generate chiral memory during temperature cycling between the SmC$_A$P$_A$ and HNF phase of an achiral bent-core LC with Iso–SmC$_A$P$_A$–HNF phase sequence observed on cooling.[142] Remarkably, (*S*,*S*)/(*S*,*S*)-9 exhibited a coexistence of left-handed HNF$_{mod2b}$s and right-handed HLNCs on slow and rapid cooling, but a SmC$_A$P$_A$ phase when an electric field (E = 18 V µm^{-1}) was applied during the Iso-HNF$_{mod2b}$/HLNC phase transition due to the introduction of the (*S*,*S*)-2,3-difluoro stereopolar units.

With respect to UV light as trigger for a phase or morphological change, compound 10 was designed with an azobenzene unit in the longer *para*-arm. Bent-core LCs with azobenzene motives forming HNFs (compound B in Scheme1) permit alignment of the HNFs[143] by taking advantage of the Weigert effect.[144] Here, after successive reversible photo-isomerization, the equilibrium state is biased toward the thermodynamically more stable *trans* isomer, which ultimately leads to a molecular orientation in the direction parallel to the impinging UV light irradiation. In the case of compound 10, these orientational effects, when UV light (λ = 365 nm) was used to irradiate the sample during the Iso-Col-HNF phase transitions, resulted in the disappearance of the HLNC morphology that coexisted with the HNF$_{mod2b}$ morphology on slow and rapid cooling. Furthermore, a likely more uniform molecular orientation in the ensuing HNFs abolished any intra- or interlayer modulation.[141] To better understand why these different morphologies form and why their physical dimensions are what was observed in the EM and AFM images, we lean on the geometric considerations in Figure 1. The overall molecular conformation of the closely related molecules C and 1 – 10 (Scheme 1 and 2) as well as the conformations at the core-chain junctures impact molecular packing and inlayer tilt (calculated from X-ray diffraction data). HNFs, HNF$_{mod}$s, and HNF$_{mod2a}$s are characterized by the smallest filament width ($w \sim$ 40 nm); the HNF$_{mod2b}$s by a greater filament width ($w \sim$ 100 nm).

Figure 10. Geometric considerations for multilayer nano- and microfilament formation in bent-core molecules: **(a)** Morphology depending on the critical width (w) of the individual filaments and (b) helical flat filament type depending on the filament tilt angle α with respect to the pitch axis. A movie showing the gradual transition between screw helix and cylindrical helix via intermediate bladed worm and Auger worm is provided in the Electronic Supporting Information (ESI)‡.

The crucial requisites of self-limiting w and t mean that the HNF$_{mod2b}$s with larger w need to consist of significantly more layers, as experimentally observed ($\sim$ 17 for HNF$_{mod2b}$s vs. 5 – 7 for HNF$_{(mod2a)}$s). As discussed in section 2.1 and shown in Figure 1, if the filament width increases further, given a quasi-identical number of sub-layers ($\sim$ 8 for HLNCs), flat filaments with larger w will preferentially adopt a cylindrical curvature resulting in cylindrical helices that will, like for many of the other classes of materials), limit the exposure of the splayed ribbon edges, eventually leading to tubular structures either with or without discernable helicoidal wrapping (Figure 10a). As w increases further, HµFs with helical multilayer filaments shaped like Auger worm form. Even larger w result in FNRs. As shown in Figure 10b, the progressive transition from screw helices to cylindrical helices only depends on the filament tilt angle α (see a movie of

Figure 11. (a) Under confinement, HNFs gradually transition from HNFs with smaller helix angle ψ and smaller p to almost a screw helix (increase in filament tilt α with respect to helix axis) with larger ψ and p. Thus, the number of smectic filament layers *N* (not shown in single-ribbon models) increases as well. **(b)** This situation was experimentally realized by confining P-9-O-PIMB (Scheme 1) in nanoporous anodic aluminum oxide (AAO) films and then varying the diameter of the pores; see EM images in panels (i) – (iii) (hp is the $p/2$). (iv) – (vi) show the grazing incidence-x-ray diffraction (GIXD) data (note the clearly visible increase in the azimuthal distribution $\Delta\chi$), and (vii) – (ix) show sketches of the layer arrangement depending on the pore diameter (note the increase in *N*). Reprinted with permission from ref. 119, Copyright 2014 National Academy of Science of the USA.

this shape transition in the Electronic Supporting Information, ESI). This transition additionally underpins that the formation of HLNCs and HμFs is related given the rather similar ribbon width.

Thus, the here described formation of all up to now discovered helical nano- and microfilaments follows the simple geometric considerations outlined for the opening of seedpods,[12] where the filament angle θ (the in-layer misfit) as well as the filament ribbon width w and thickness t regulate the final morphology.

Considering the variety of shapes reported thus far, surprisingly absent are screw helices. As indicated in Figure 10b and 11a, all that would be required is a further deformation of the flat filament until a filament tilt angle α = 90° (equal to the helix angle ψ = 90°) is reached. By confining HNFs in nanoporous anodic aluminum oxide (AAO) films and further varying the pore diameter from 20 to 80 nm (some shown in Figure 11b), HNFs with $\alpha = \psi = 61°$ were generated (panels (i) – (iii); Figure 11b). With the additional space in pores of d_{AAO} = 80 nm available for HNF formation, the number of smectic layers, *N*, also increased with increasing d_{AAO} (panels (vii) – (ix) in Figure 11b).[119] Finally, recent work indicated that helical nano- and microfilaments can be logically blended in 1:1 mixtures of bent-core molecules forming different filament morphologies. These experiments showed that the type of filament as well as the handedness can

Figure 12. (a) Using Gemini surfactant 16-2-16 (L-tartrate) as template for GNP helical assembly after silicification first with TEOS (see Figure 3a) and functionalization with APTES (aminopropyltriethoxysilane): (i) TEM image of the resulting GNP helix, (ii) model, (iii) and (iv) cross-sectional and longitudinal slices imaged by electron tomography. Reprinted with permission from ref. 146, Copyright 2017 American Chemical Society. **(b)** SEM and TEM (insets) images of helical carbon nanofibers (HCNFs) with embedded Fe and Fe_3C and (ii) Fe_3O_4 nanoparticles starting with the pyrolysis of ferrocene to obtain (i) and after oxidation in a CO_2 atmosphere to obtain (ii). Reprinted with permission from ref. 148, Copyright 2012 Wiley-VCH. **(c)** (i) – (iii) TEM images of Pd nanocrystals self-assembled onto HCNFs after surface modification of the HCNFs with benzyl mercaptan followed by addition of Pd acetate and reduction with hydrazine. Reprinted with permission from ref. 149, Copyright 2012 Elsevier. **(d)** Experiment to show that HCFs behave like elastic springs when clamped between two AFM cantilevers: (i) the left one is stiffer than the one in the right, (ii) relaxed HCF, and (iii), (iv) at 20% and 33% elongation, respectively. Reprinted with permission from ref. 151, Copyright 2003 American Chemical Society. **(e)** Formation of a GNP helix using a gold-binding oligopeptide conjugate ($C_{18}H_{37}$-AYSSGAPPMPPF = C18-PEP_{AU}): (i) model and assembly process of the cylindrical helical ribbon formed by this oligopeptide, (ii) AFM and (iii) TEM image, and (iv) single-helix assembly model. Reprinted with permission from ref. 154, Copyright 2016 American Chemical Society. **(f)** Double-helical assembly of GNPs using $C_{12}H_{25}$-AYSSGAPPMPPF (C12-PEP_{AU}): (i) – (iv) TEM images showing the double left-handed helix formed by the GNPs, and (v) schematic showing the assembly. Reprinted with permission from ref. 155, Copyright 2008 American Chemical Society. **(g)** Use of ferrocene oligopeptide conjugates to generate left- and right-handed silica nanoribbons after treatment with TEOS and trimethoxysilylpropyl-N,N,N-trimethylammonium chloride (TMAPS): (i) chemical structure of ferrocene peptides (ferrocene-^{L}Phe-(^{L}Phe)-(^{L}Phe)-OH; see also Figure 7e), (ii) self-assembly, silicification, and calcination, (iii) – (vii) SEM + TEM images and model of left-handed twisted ribbons in 10% acetonitrile in H_2O, (viii) – (xii) SEM and TEM images, as well as a model, of the right-handed twisted ribbons in 10% isopropanol in H_2O. Reprinted with permission from ref. 157, Copyright 2018 Wiley-VCH.

be a priori predicted by assuming the ensuing sum (or the average) chemical structure of the two bent core molecule components. For example, a physical blend of (*S*)-2 (forming left-handed HμFs) and (*S*)-3 (that forms right-handed HLNCs) will form left-handed HNFs just like (*S*,*S*)-1 (Scheme1).[145]

3. Use as templates for applications

Given the ubiquitous nature of chiral nano- and microfilaments across these various material platforms and further armed with knowledge of the common driving forces for their formation, largely based on simple geometric considerations, this section will provide a brief overview over the use of such filaments as a template for other materials.

Figure 13. (a) Formation of helical gold nanomaterial superstructures: (i) GNP (Au2) capped with a mixed ligand shell of $—SC_{12}H_{25}$ and a pro-mesogenic ligand that is structurally similar to the dimeric bent-core mesogen (a phenylbenzoate dimer analogue of B in Scheme 1), (ii) TEM image of heat-annealed Au2, (iii) and (iv) double helical GNP superstructure formed around HNF template (assembling at the exposed aromatic sublayers of the HNFs), (v) GNR capped with the same promesogenic ligand (Au3), (vi) TEM of Au3, (vii) and (viii) TEM images revealing the GNR superstructure formed around HNF template, (ix) hierarchical self-assembly of dendritic growth by HNF-GNR superhelices, and (x) 3-D reconstruction from TEM images. Reprinted with permission from ref. 158, Copyright 2020 Wiley-VCH. **(b)** (i) TEM images of the double-helical organization of gold nanoparticles differing in size and shape and (ii) corresponding 3-D models. Reprinted with permission from ref. 159, Copyright 2022 Wiley-VCH. **(c)** Demonstration of the reflective optical properties of HNFs formed by B: (i) POM images of shadowed and UV-irradiated areas, (ii) schematic of the selective reflection, (iii) reflected color (against dark background) based on aliphatic spacer length n (n = 5, 7, 9, and 11 for compound B; see Scheme2) and (iv) color against light background. Reprinted with permission from ref. 143, Copyright 2019 Springer Nature. **(d)** Using adjacent left- and right-handed UV-aligned HNF domains formed by compound B (n = 9, Scheme 1) to create a chirality sensor (here for carbohydrates): (i) and (ii) concept, (iii) and (iv) chirality and opposite rotation of plane-polarized light detected for the two carbohydrates (levorotatory (−)-fructose and dextrorotatory (+)-glucose) when viewed through a quarter-wave plate and linear polarizer, and (v) no chiral domains visible in the presence of an achiral analyte (here, just H_2O). Reprinted with permission from ref. 167, Copyright 2019 Wiley-VCH. **(e)** (i) – (iv) fabrication process for a chiral physical unclonable function (PUF) based on HNFs formed by compound B (Scheme 1) as a photonic crystal. Reprinted with permission from ref. 168, Copyright 2022 Royal Society of Chemistry.

With noble metal nanoparticles frequently being prime targets for their helical assembly, given their technologically important optical and electronic properties, the example shown in Figure 12a is highly representative for a wide range of chiral templating strategies. As shown already in Figure 3a(iii), Gemini surfactants such as 16-2-16 (L)-tartrate, can serve as the initial template for a solid silica replica of the cylindrical helix formed by the Gemini surfactant. Subsequent removal of the surfactant and reaction of with appropriately functionalized gold nanoparticles (GNPs) led to tunable and robust GNP nanohelices. Tunability is here achieved, for example, by selecting the desired configuration of the tartrate counterion. L-tartrate at the first templating step ultimately leads to left-handed GNP nanohelices, D-tartrate to right-handed ones.[146] While not precise with respect to GNP pitch and placement as those generated by DNA origami,[147] this double-templating strategy is straightforward and scalable.

HCNFs nucleate during the decomposition of acetylene on iron and iron carbide (cementite, Fe_3C) nanoclusters (Figure 5b).[53] Using ferrocene as the source for C and Fe, pyrolysis at 700 °C in an Ar atmosphere directly results in HCNFs with embedded Fe or, after subsequent oxidation at 700 °C in a CO_2 atmosphere, to embedded Fe_3O_4 clusters that follow the helical nature of the in-situ generated HCNF template. The composites generated in this simple, low-cost process were further tested and showed promise as anode materials for Li-ion batteries.[148] Another path to NP-decorated HCNFs follows a more traditional templating approach. Readily prepared HCNFs are first functionalized with benzyl mercaptan, which binds to the walls via π-π interactions, and Pd nanoparticles are grown directly onto the thiol surface groups via reduction of a Pd(II) precursor (Figure 12c).[149, 150]

With Pd as a metal, the final composites were tested as catalysts for fuel cells.[149] What works for Pd as a metal should also work for Au. If combined with the elastic deformation of HCFs, as shown in Figure 12d using two AFM cantilevers,[151] the resulting filaments could be used for tunable optical metamaterials.

Single and double GNP helices were also generated using Au-binding oligopeptide[152, 153] amphiphiles as cylindrical helical or twisted ribbon (helicoidal) templates. As emphasized in Figure 7a-d, oligopeptide amphiphiles, depending on a combination of chemical structure and experimental conditions (e.g., solvent), form almost the entire gamut of filament morphologies, from helicoids to tubules. Circular helical ribbons then led to single GNP-helices (Figure 12e),[154] whereas helicoids were engaged to generate GNP-double helices (Figure 12f).[155] Remarkable is the dual function of the Au-binding oligopeptide motif ($\mathrm{PEP}_{\mathrm{AU}}$) as binder for the GNPs while aiding the self-assembly of the active template.[156] Another example of such solvent-controlled self-assembly and templating mechanism was shown for ferrocene oligopeptides such as ferrocene-($^{\mathrm{L}}$Phe)$_n$-OH (n = 1,2, or 3, Figure 12g).[157] Just as shown for the Gemini surfactants in Figure 12a, silicification of ferrocene-based oligopeptides using a silane and an ionic silyl halide (using the dipeptide ferrocene-($^{\mathrm{L}}$Phe)$_2$-OH, panel (ii); Figure 12g) leads to solid left- (panels (iii) – (vii), Figure 12g) or right-handed helicoids (panels (viii) – (xii); Figure 12g) with the observed handedness affected by the choice of solvent mixture composition.[157]

Double helical nanoparticle assemblies closely related to those provided in Figure 12 for oligopeptide-, carbon- or surfactant-based materials as chiral templates were also realized for HNFs especially once the GNPs (here also GNRs) were capped with ligands that mimicked the chemical structure of the bent-core LC forming the HNFs (Figure 13a and b).[158-160] Decoration of nanoparticles with pro-mesogenic ligands, often recognized as a prerequisite for initially required good dispersion of NPs,[161-164] leads to multilevel hierarchical assemblies beginning with parallel rows of GNPs or GNRs all the way to dendritic growth of HNF-double helical GNPs (or GNRs) composites.[158] For further generation of active plasmonics with tunable plasmonic circular dichroism (PCD), PCD intensity as well as the spectral position (wavelength) can be finetuned using Au nanomaterials differing in size and shape as well as using increasing concentrations of chiral solutes to tune HNF pitch and handedness.[159]

Taking advantage of the porous nature of HNF assemblies and the fact that HNFs expel guests quite proficiently,[165] HNFs have been used as templates not only for plasmonic nanomaterials but also for carbon-based nanomaterials such as fullerenes. Using flash-photolysis time-resolved microwave conductivity (TRMC) measurements in samples where the HNF phase formed by P-9-O-PIMB (see Scheme 1) was used to fabricate C_{60}-based heterojunctions, the working principle of prototypical electron acceptors for organic photovoltaics was demonstrated.[166]

Benefitting from the inherent chiral shape and properties of HNFs, HNFs formed by compound B (Scheme 1, with n = 5, 7, 9, and 11) were shown to permit the generation of wavelength-specific structural color reflectors after UV alignment. With the value of the HNF helical pitch dependent on the aliphatic tether length, n, the reflected structural color could be tuned from $\lambda \sim$ 450 – 550 nm, and these reflected colors could further be patterned using photomasks (Figure 13c).[143] The same HNF material (B with n = 9, Scheme 1), after UV photoalignment of the HNFs perpendicular to the confining substrates, was used to design a chirality detector for carbohydrates (as example). The chiral photonic HNF films serve as the source for left- and right-handed circularly polarized visible light. When combined with a quarter wave plate ($\lambda/4$) as well as a linear polarizer (P), levo- or dextrorotation of (−)-fructose and (+)-glucose, respectively, could be imaged by microscopy (the orange cylinder in Figure 13d represents the carbohydrate solutions in glass cylinders).[167]

The final example in Figure 13f depicts how the photonic crystal colors of HNFs were employed to create physical unclonable functions (PUFs) for security and anticounterfeit applications. With the proven concept of HNF alignment by UV light using azobenzene flexible dimer HNF materials (like compound B) and patterned photomasks, complex pattern such as QR codes were generated with a final encoding capacity of $E_{256} \sim 10^{13,000}$, which could take brute force algorithms $\sim 10^{199}$ years to simulate or predict.[168]

Helical nano- and microfilaments are also exceptionally tunable templates for the generation of circular polarized luminescence (CPL) sought after for numerous applications in optical information storage and encryption.[169-175]

Figure 14. (a) (i) and (ii) Concept of generating circularly polarized luminescence (CPL) using nano- or microfilament morphologies. Concentration-dependent $|g_{lum}|$ values of (*R*,*R*)-1 (Scheme 1) with the double-helical assembled aggregation-induced emission (AIE) dye hexaphenylsilole (HPS). (iv) and (v) alignment in AAO nanoporous films leads to an increase in $|g_{lum}|$, here using (*S*,*S*)-1 (see Scheme 1). Reprinted and adapted with permission from ref. 186, Copyright 2022 American Chemical Society. **(b)** Generation of CPL using P-18-O-PIMB (n = 18, see Scheme 1) using a chiral dopant to create left-or right-handed HNFs and double-helically assembled InP/ZnS quantum dots (QDs): (i) formation of HNFs and co-assembly of QDs from the melt, (ii) detected energy transfer from the organic HNFs to the QDs, and (iii) g_{lum} plotted vs. wavelength in nm depending on the HNF handedness and QD concentration (QD2: 4.5 wt%; QD4: 8.5 wt%). Reprinted with permission from ref. 187, Copyright 2022 American Chemical Society.

To benchmark CPL efficiency is to calculate the luminescence dissymmetry factor $g_{lum} = 2(I_L - I_R)/(I_L + I_R)$, where I_L and I_R are the intensity of the left- and right-handed circularly polarized luminescence, respectively.[176-181] Thus, the values of g_{lum}, by definition, range from +2 to −2.

The maximum value of $|g_{lum}|$ = 2 means that an ideal left- or right-handed polarization of the emitted light, while a g_{lum} = 0 corresponds to no CPL. Hence, photophysical property of CPL echoes structural information of chiral molecules or molecules in chiral environments in their excited states, and chiral nano- or microfilaments are ideal candidates based on overall tunable shapes and dimensions (across the various materials platforms described here). Most organic CPL systems tested in solution show $|g_{lum}|$ values in the range of 10^{-5} to 10^{-3} in magnitude[182] and their performance is often diminished in the solid state due to the notorious aggregation-caused quenching (ACQ) effect. Thus, design and preparation of chiral AIE systems[183-185] (light emission induced by aggregate formation) was selected as one possible approach to address this problem (Figure 14a). All five helical filament morphologies showed intrinsic CPL activity on the order of 10^{-3} to 10^{-2} with the HNF$_{mod2a}$s formed by compounds (*S*,*S*)-1 or (*R*,*R*)-1 returning the highest values for $|g_{lum}|$ since this particular HNF$_{mod2a}$ morphology features the tightest pitch, p.

As for the mesogen-functionalized Au2 and Au3 (Figure 13a), HPS aggregates at HNF faces exposing aromatic sublayers in a double-helical fashion. The calculated $|g_{lum}|$ is then also the highest when HPS is mixed with the HNF$_{mod2a}$s until a maximum concentration of about 0.2 wt% is reached (panel (iii), Figure 14a). A further increase in HPS concentrations leads to HPS self-aggregation and lower values for $|g_{lum}|$. A further increase in $|g_{lum}|$ up to $|g_{lum}|$ = 0.25 was anticipated and observed when the HNF$_{mod2a}$s were aligned in AAO with d_{AAO}= 60 nm (panels (iv) and (v); Figure 14a).[186]

A final illustration of CPL generated through the chiral assembly of quantum dots (QDs) in a double-helical formation around HNFs is presented in Figure 14b. Using an axially chiral dopant, left- or right-handed HNFs served as chiral template for InP/ZnS QDs. The calculated $|g_{lum}|$ values were one order of magnitude lower than for the AIE dye HPS ($|g_{lum}|$ on the order of 10^{-2}) perhaps due to some degree of luminescence quenching once the QDs decorate the HNFs at QD concentrations reaching up to 8.5 wt%.[187]

The examples discussed here in more details are, of course, only emblematic for the wide range of possible or already realized applications for chiral nano- and microfilaments. Not any less noteworthy are applications ranging from sensing[188, 189] to (bio)-medical uses.[190-192]

4. Conclusions

The creation, investigation, and application-driven use of chiral organic as well as inorganic nano- and microfilaments remain very active and attractive fields of research.[58, 193-199] While this review specifically focused on developing an understanding of what ultimately leads to chiral twisting and writhing in organic materials, their use as templates for inorganic nanomaterials or emitters aimed at a wide range of applications will continue to drive research in this expanding field.

Notable, given the geometric approach of intra- or interlayer misfits, is the comparatively scarce manifestation of flat ribbon-based on Archimedes-type screw helices with the filament tilt angle approaching α = 90°. One such rare example is shown in Figure 15. In this case, the ferrocene-(^{L}Phe)$_2$-OH dipeptide that we have seen earlier in this review (Figure 7e and 12g)—capable of growing a range of filament types—under specific conditions generated multi-helical fibers around which a screw helix ribbon formed.[200]

Figure 15. Example of a rarely observed screw helix (Archimedes screw filament) formed by (i) ferrocene-(^{L}Phe)$_2$-OH. Considering the phase diagram (plotting counterion rigidity vs. medium polarity index) shown in panel (ii), the unique growth of a screw helix around or along with twisted nanohelices (see model in (iii) and SEM images in (iv) and (v)) leads to larger hierarchical structures (several µm in length and over 1 µm in width) that are rigid and can only be generated by very specific conditions (i.e., choice of counterion, temperature, pH, solvent mixture polarity, structurally rigid ammonium salt additives such as a piperazine buffer solution). Reprinted with permission from ref. 200, Copyright 2015 American Chemical Society.

Given the large number of known polycyclic aromatic molecules with a screw helical shape (helicenes[201-204]), the fact that screw helices are rare among organic nano- and microfilaments is likely related to the types of deformations required to generate screw helices in organic self-assembled system. To form a screw helix, a combination of continuous splay, if anisometric building blocks arrange parallel to the ribbon width, or continuous bend, if such building blocks are parallel to the ribbon height, and a continuous twist along the helix axis are needed. A larger ribbon width would be necessary to accommodate such deformations, as seen for the ∼ 500 nm wide ribbons in Figure 15 (panels (iv) and (v)). At such larger widths, flat multilayer ribbons are stable, competing favorably with such screw helices as shown for some materials systems in this review already (Figure 3b(vii), Figure 7c(ii), and compounds (*R*,*R*)-6 as well as (*R*)-7 in Scheme 2). Nature's helices[205] will continue to be a source of inspiration for mathematicians, biologists, physicists, chemists, and engineers to continue finding material systems that combine chiral shape with functionality, since these two concepts appear intricately linked to one another.[206-208] We also want to leave the reader with a number of previously published reviews and key articles in this exciting field. These include several outstanding articles by Liu et al. on the formation of helical nanostructures in a variety of material systems,[209-212] reviews by Shimizu et al., Aida and Meijer, as well as Bhosale et al. on supramolecular helical architectures,[213-215] and finally several overview articles on chiral superstructures in liquid crystals.[216-220] The omnipresence of chiral nano- and microfilaments coupled with myriad lucrative applications are major reasons why we should stay tuned!

Author Contributions

All authors contributed to a varying extent to the write-up of this review.

Conflicts of interest

There are no conflicts to declare.

Acknowledgements

A portion of the work by the authors on bent-core helical nano- and microfilament formation discussed in this review was financially supported by the U.S. National Science Foundation (NSF; DMR-1506018, CHE-1659571, DMR-1904091) and by the Ohio Third Frontier program for Ohio Research Scholars "Research Cluster on Surfaces in Advanced Materials" (T.H.).

Notes and references

‡ A movie showing the gradual transition between a screw helix and a cylindrical helix depending on the ribbon tilt angle with respect to the helix axis (α) is shown in the Electronic Supporting Information (ESI).

1. J. G. Miller, S. A. Hughes, C. Modlin and V. P. Conticello, *Quart. Rev. Biophys.*, 2022, **55**, e2, 1-39.
2. A. W. P. Fitzpatrick, B. Falcon, S. He, A. G. Murzin, G. Murshudov, H. J. Garringer, R. A. Crowther, B. Ghetti, M. Goedert and S. H. W. Scheres, *Nature*, 2017, **547**, 185-190.
3. D. Kurouski, X. F. Lu, L. Popova, W. Wan, M. Shanmugasundaram, G. Stubbs, R. K. Dukor, I. K. Lednev and L. A. Nafie, *J. Am. Chem. Soc.*, 2014, **136**, 2302-2312.
4. T. Izore, D. Kureisaite-Ciziene, S. H. McLaughlin and J. Lowe, *eLife*, 2016, **5**, e21600.
5. D. M. Bassen, Y. Hou, S. S. Bowser and N. K. Banavali, *Sci. Rep.*, 2016, **6**, 31723.
6. C. H. S. Aylett, Q. Wang, K. A. Michie, L. A. Amos and J. Lowe, *Proc. Natl. Acad. Sci. USA*, 2010, **107**, 19766-19771.
7. M. A. Constantino, M. Jabbarzadeh, H. C. Fu and R. Bansil, *Sci. Adv.*, 2016, **2**, 1601661.
8. I. Gutsche, A. Desfosses, G. Effantin, W. L. Ling, M. Haupt, R. W. H. Ruigrok, C. Sachse and G. Schoehn, *Science*, 2015, **348**, 704-707.
9. M. C. S. Kingsley and M. A. Ramsay, *Arctic*, 1988, **41**, 236-238.
10. Y. C. Zhang, W. Huang, C. Hayashi, J. Gatesy and J. McKittrick, *J. R. Soc. Interface*, 2018, **15**, 20180093.
11. J. S. Wang, G. Wang, X. Q. Feng, T. Kitamura, Y. L. Kang, S. W. Yu and Q. H. Qin, *Sci. Rep.*, 2013, **3**, 3102.
12. S. Armon, E. Efrati, R. Kupferman and E. Sharon, *Science*, 2011, **333**, 1726-1730.
13. N. M. Larson, J. Mueller, A. Chortos, Z. S. Davidson, D. R. Clarke and J. A. Lewis, *Nature*, 2023, **613**, 682-688.
14. H. Golasz-Szolomicka and J. Szolomicki, *IOP Conf. Ser.-Mat. Sci.*, 2019, **471**, 052050.
15. F. Wang, X. Y. Yue, Q. Ding, H. W. Lin, C. L. Xu and S. Li, *Nanoscale*, 2023, **15**, 2541-2552.
16. J. J. Pelayo, I. Valencia, A. P. Garcia, L. Chang, M. Lopez, D. Toffoli, M. Stener, A. Fortunelli and I. L. Garzon, *Adv. Phys. X*, 2018, **3**, 965-998.
17. L. Xiao, T. T. An, L. Wang, X. L. Xu and H. D. Sun, *Nano Today*, 2020, **30**, 100824.
18. S. Pieraccini, S. Masiero, A. Ferrarini and G. P. Spada, *Chem. Soc. Rev.*, 2011, **40**, 258-271.
19. J. P. F. Lagerwall, C. Schutz, M. Salajkova, J. Noh, J. H. Park, G. Scalia and L. Bergstrom, *NPG Asia Mater.*, 2014, **6**, e80.
20. T. Gibaud, E. Barry, M. J. Zakhary, M. Henglin, A. Ward, Y. S Yang, C. Berciu, R. Oldenbourg, M. F. Hagan, D. Nicastro, R. B. Meyer and Z. Dogic, *Nature*, 2012, **481**, 348-351.
21. S. Armon, H. Aharoni, M. Moshe and E. Sharon, *Soft Matter*, 2014, **10**, 2733-2740.
22. Y. Forterre and J. Dumais, *Science*, 2011, **333**, 1715-1716.
23. G. M. Grason, *J. Chem. Phys.*, 2016, **145**, 110901.
24. G. M. Grason, *Soft Matter*, 2020, **16**, 1102-1116.
25. D. M. Hall and G. M. Grason, *Interface Focus*, 2017, **7**, 20160140.
26. R. L. B. Selinger, J. V. Selinger, A. P. Malanoski and J. M. Schnur, *Phys. Rev. Lett.*, 2004, **93**, 158103.
27. R. V. Kohn and E. O'Brien, *J. Elasticity*, 2018, **130**, 115-143.
28. P. K. Agarwal, H. Edelsbrunner and Y. Wang, *Discrete Comput. Geom.*, 2004, **32**, 37-53.
29. R. Oda, I. Huc, M. Schmutz, S. J. Candau and F. C. MacKintosh, *Nature*, 1999, **399**, 566-569.
30. A. Brizard, C. Aime, T. Labrot, I. Huc, D. Berthier, F. Artzner, B. Desbat and R. Oda, *J. Am. Chem. Soc.*, 2007, **129**, 3754-3762.
31. N. Ryu, Y. Okazaki, K. Hirai, M. Takafuji, S. Nagaoka, E. Pouget, H. Ihara and R. Oda, *Chem. Commun.*, 2016, **52**, 5800-5803.
32. J. H. Fuhrhop and W. Helfrich, *Chem. Rev.*, 1993, **93**, 1565-1582.
33. Z. Dogic and S. Fraden, *Curr. Opin. Colloid Interf. Sci.*, 2006, **11**, 47-55.

34. A. B. Petrova, C. Herold and E. P. Petrov, *Soft Matter*, 2017, **13**, 7172-7187.
35. F. B. Wang, V. Cvirkaite-Krupovic, M. Vos, L. C. Beltran, M. A. B. Kreutzberger, J. M. Winter, Z. L. Su, J. Liu, S. Schouten, M. Krupovic and E. H. Egelman, *Cell*, 2022, **185**, 1297-1307.
36. R. Jones, S. Fraden and I. Hamley, *Philos. Trans. Roy. Soc. A*, 2001, **359**, 1014-1015.
37. W. R. Davis, R. J. Slawson and G. R. Rigby, *Nature*, 1953, **171**, 756-756.
38. S. Iijima, *Nature*, 1991, **354**, 56-58.
39. D. C. Wang, Y. Lei, W. Jiao, Y. F. Liu, C. H. Mu and X. Jian, *Rare Metals*, 2021, **40**, 3-19.
40. H. Raghubanshi, E. D. Dikio and E. B. Naidoo, *J. Ind. Eng. Chem.*, 2016, **44**, 23-42.
41. A. Shaikjee and N. J. Coville, *J. Adv. Res.*, 2012, **3**, 195-223.
42. A. C. Dupuis, *Prog. Mater. Sci.*, 2005, **50**, 929-961.
43. B. I. Dunlap, *Phys. Rev. B*, 1992, **46**, 1933-1936.
44. S. Ihara and S. Itoh, *Carbon*, 1995, **33**, 931-939.
45. A. Fonseca, K. Hernadi, J. B. Nagy, P. Lambin and A. A. Lucas, *Carbon*, 1995, **33**, 1759-1775.
46. N. M. Rodriguez, A. Chambers and R. T. K. Baker, *Langmuir*, 1995, **11**, 3862-3866.
47. C. N. Ramachandran and N. Sathyamurthy, *Curr. Sci. India*, 2006, **91**, 1503-1505.
48. J. Y. Wu, J. Y. He, G. M. Odegard, S. Nagao, Q. S. Zheng and Z. L. Zhang, *J. Am. Chem. Soc.*, 2013, **135**, 13775-13785.
49. P. R. Bandaru, C. Daraio, K. Yang and A. M. Rao, *J. Appl. Phys.*, 2007, **101**, 094307.
50. X. Chen, S. Motojima and H. Iwanga, *J. Cryst. Growth*, 2002, **237**, 1931-1936.
51. J. B. Cheng, J. H. Du and S. Bai, *New Carbon Mater.*, 2009, **24**, 354-358.
52. S. Yang, X. Chen and S. Motojima, *J. Mater. Sci.*, 2004, **39**, 2727-2736.
53. N. J. Tang, J. F. Wen, Y. Zhang, F. X. Liu, K. J. Lin and Y. W. Du, *ACS Nano*, 2010, **4**, 241-250.
54. Y. Qin, Z. K. Zhang and Z. L. Cui, *Carbon*, 2004, **42**, 1917-1922.
55. X. Liu, G. Licht and S. Licht, *Mater Today Chem*, 2021, **22**.
56. Y. Y. Shang, Y. B. Li, X. D. He, S. Y. Du, L. H. Zhang, E. Z. Shi, S. T. Wu, Z. Li, P. X. Li, J. Q. Wei, K. L. Wang, H. W. Zhu, D. H. Wu and A. Y. Cao, *ACS Nano*, 2013, **7**, 1446-1453.
57. K. W. Huang, Y. R. Wu, K. U. Jeong and S. W. Kuo, *Macromol. Rapid Commun.*, 2013, **34**, 1530-1536.
58. R. A. Scanga and J. F. Reuther, *Polym. Chem.*, 2021, **12**, 1857-1897.
59. Y. M. Hu, S. J. Teat, W. Gong, Z. Zhou, Y. H. Jin, H. X. Chen, J. Y. Wu, Y. Cui, T. Jiang, X. B. Cheng and W. Zhang, *Nat. Chem.*, 2021, **13**, 660-665.
60. B. Brodsky and A. V. Persikov, *Adv. Protein Chem.*, 2005, **70**, 301-339.
61. J. V. Selinger, R. L. B. Selinger, S. K. Jha and M. M. Green, *Chirality*, 1998, **10**, 41-45.
62. I. G. Bak, C. G. Chae and J. S. Lee, *Macromolecules*, 2022, **55**, 1923-1945.
63. S. Mayer and R. Zentel, *Prog. Polym. Sci.*, 2001, **26**, 1973-2013.
64. F. Freire, E. Quinoa and R. Riguera, *Chem. Rev.*, 2016, **116**, 1242-1271.
65. C. H. Cai, J. P. Lin, T. Chen, X. S. Wang and S. L. Lin, *Chem. Commun.*, 2009, 2709-2711.
66. A. Niehoff, A. Mantion, R. McAloney, A. Huber, J. Falkenhagen, C. M. Goh, A. F. Thunemann, M. A. Winnik and H. Menzel, *Colloid Polym. Sci.*, 2013, **291**, 1353-1363.
67. T. N. Zhao, Y. S. Zheng, X. M. Zhang, D. F. Teng, Y. Q. Xu and Y. C. Zeng, *Mater. & Design*, 2021, **205**, 109705
68. L. Q. Wang and J. P. Lin, *Soft Matter*, 2011, **7**, 3383-3391.
69. Y. Yang, J. Liang, F. Pan, Z. Wang, J. Q. Zhang, K. Amin, J. Fang, W. J. Zou, Y. L. Chen, X. H. Shi and Z. X. Wei, *Nat. Commun.*, 2018, **9**, 3808.
70. D. Amsallem, A. Bedi, F. Tassinari and O. Gidron, *Macromolecules*, 2020, **53**, 9521-9528.
71. C. Q. Zhou, X. H. Sun and J. Han, *Mater. Chem. Front.*, 2020, **4**, 2499-2516.
72. L. A. P. Kane-Maguire and G. G. Wallace, *Chem. Soc. Rev.*, 2010, **39**, 2545-2576.
73. D. Kotkar, V. Joshi and P. K. Ghosh, *J. Chem. Soc. Chem. Comm.*, 1988, 917-918.
74. D. Li, J. X. Huang and R. B. Kaner, *Acc. Chem. Res.*, 2009, **42**, 135-145.
75. Y. Zhang, B. Xia, Y. J. Hu, Q. Y. Zhu, X. F. Lin and Q. Wu, *ACS Macro Lett.*, 2019, **8**, 1188-1193.
76. K. Okoshi, S. Sakurai, S. Ohsawa, J. Kuniaki and E. Yashima, *Angew. Chem. Int. Edit.*, 2006, **45**, 8173-8176.
77. I. Louzao, J. M. Seco, E. Quinoa and R. Riguera, *Angew. Chem. Int. Edit.*, 2010, **49**, 1430-1433.
78. K. Akagi, G. Piao, S. Kaneko, K. Sakamaki, H. Shirakawa and M. Kyotani, *Science*, 1998, **282**, 1683-1686.
79. K. Akagi, T. Yamashita, K. Horie, M. Goh and M. Yamamoto, *Adv. Mater.*, 2020, **32**, 1906665.
80. K. Akagi, S. Guo, T. Mori, M. Goh, G. Piao and M. Kyotani, *J. Am. Chem. Soc.*, 2005, **127**, 14647-14654.
81. K. Akagi, *Chem. Rev.*, 2009, **109**, 5354-5401.
82. S. Matsushita, B. R. Yan, S. Yamamoto, Y. S. Jeong and K. Akagi, *Angew. Chem. Int. Edit.*, 2014, **53**, 1659-1663.
83. T. Mori, A. Sharma and T. Hegmann, *ACS Nano*, 2016, **10**, 1552-1564.
84. A. Nemati, S. Shadpour, L. Querciagrossa, T. Mori, C. Zannoni and T. Hegmann, *ACS Nano*, 2019, **13**, 10312-10326.
85. I. W. Hamley, *Angew. Chem. Int. Edit.*, 2014, **53**, 6866-6881.
86. C. M. Dobson, *Nature*, 2003, **426**, 884-890.
87. J. T. Marinko, H. Huang, W. D. Penn, J. A. Capra, J. P. Schlebach and C. R. Sanders, *Chem. Rev.*, 2019, **119**, 5537-5606.
88. J. Adamcik, V. Castelletto, S. Bolisetty, I. W. Hamley and R. Mezzenga, *Angew. Chem. Int. Edit.*, 2011, **50**, 5495-5498.
89. S. Bolisetty, J. Adamcik and R. Mezzenga, *Soft Matter*, 2011, **7**, 493-499.
90. I. W. Hamley, A. Dehsorkhi, V. Castelletto, S. Furzeland, D. Atkins, J. Seitsonen and J. Ruokolainen, *Soft Matter*, 2013, **9**, 9290-9293.
91. H. Cui, T. Muraoka, A. G. Cheetham and S. I. Stupp, *Nano Lett.*, 2009, **9**, 945-951.
92. Y. R. Zhao, W. Yang, D. Wang, J. Q. Wang, Z. Y. Li, X. Z. Hu, S. King, S. Rogers, J. R. Lu and H. Xu, *Small*, 2018, **14**, 1703216.
93. Y. R. Zhao, X. Z. Hu, L. M. Zhang, D. Wang, S. M. King, S. E. Rogers, J. Q. Wang, J. R. Lu and H. Xu, *J. Colloid Interf. Sci.*, 2021, **583**, 553-562.
94. Y. F. Wang, Q. Li, J. X. Zhang, W. Qi, S. P. You, R. X. Su and Z. M. He, *ACS Nano*, 2021, **15**, 9827-9840.

95. A. Nandakumar, Y. Ito and M. Ueda, *J. Am. Chem. Soc.*, 2020, **142**, 20994-21003.

96. E. Yashima, N. Ousaka, D. Taura, K. Shimomura, T. Ikai and K. Maeda, *Chem. Rev.*, 2016, **116**, 13752-13990.

97. C. Tschierske, *Isr. J. Chem*,. 2012, **52**, 935-959.

98. T. G. Barclay, K. Constantopoulos and J. Matisons, *Chem. Rev.*, 2014, **114**, 10217-10291.

99. Y. X. Gao, J. Hao, J. D. Wu, Y. Li, Y. Lin, J. Hu and Y. Ju, *Soft Matter*, 2016, **12**, 8979-8982.

100. J. Hu, L. Gao, Y. L. Zhu, P. Y. Wang, Y. Lin, Z. Y. Sun, S. Yang and Q. Wang, *Chem.-Eur. J.*, 2017, **23**, 1422-1426.

101. S. Goskulwad, D. D. La, M. Al Kobaisi, S. V. Bhosale, V. Bansal, A. Vinu, K. Ariga and S. V. Bhosale, *Sci. Rep.*, 2018, **8**, 11220.

102. S. P. Goskulwad, M. Al Kobaisi, D. D. La, R. S. Bhosale, M. Ratanlal, S. V. Bhosale and S. V. Bhosale, *Chem.-Asian J.*, 2018, **13**, 3947-3953.

103. S. M. Wagalgave, S. D. Padghan, M. D. Burud, M. Al Kobaisi, D. D. La, R. S. Bhosale, S. V. Bhosale and S. V. Bhosale, *Sci. Rep.*, 2019, **9**, 12825.

104. S. Gim, G. Fittolani, Y. Nishiyama, P. H. Seeberger, Y. Ogawa and M. Delbianco, *Angew. Chem. Int. Edit.*, 2020, **59**, 22577-22583.

105. I. Dozov and G. R. Luckhurst, *Liq. Cryst.*, 2020, **47**, 2098-2115

106. E. T. Samulski, A. G. Vanakaras and D. J. Photinos, *Liq. Cryst.*, 2020, **47**, 2092-2097.

107. M. Čopič and A. Mertelj, *Phys. Rev. E*, 2020, **101**, 022704.

108. R. Walker, D. Pociecha, J. M. D. Storey, E. Gorecka and C. T. Imrie, *Chem.-Eur. J.*, 2019, **25**, 13329-13335.

109. V. P. Panov, S. P. Sreenilayam, Y. P. Panarin, J. K. Vij, C. J. Welch and G. H. Mehl, *Nano Lett.*, 2017, **17**, 7515-7519.

110. E. Gorecka, N. Vaupotic, A. Zep, D. Pociecha, J. Yoshioka, J. Yamamoto and H. Takezoe, *Angew. Chem. Int. Edit.*, 2015, **54**, 10155-10159.

111. V. Borshch, Y. K. Kim, J. Xiang, M. Gao, A. Jakli, V. P. Panov, J. K. Vij, C. T. Imrie, M. G. Tamba, G. H. Mehl and O. D. Lavrentovich, *Nat. Commun.*, 2013, **4**, 2635.

112. D. Chen, J. H. Porada, J. B. Hooper, A. Klittnick, Y. Q. Shen, M. R. Tuchband, E. Korblova, D. Bedrov, D. M. Walba, M. A. Glaser, J. E. Maclennan and N. A. Clark, *Proc. Natl. Acad. Sci. USA*, 2013, **110**, 15931-15936.

113. J. P. Abberley, R. Killah, R. Walker, J. M. D. Storey, C. T. Imrie, M. Salamonczyk, C. H. Zhu, E. Gorecka and D. Pociecha, *Nat. Commun.*, 2018, **9**, 228.

114. H. Hahn, C. Keith, H. Lang, R. A. Reddy and C. Tschierske, *Adv. Mater.*, 2006, **18**, 2629-2633.

115. L. E. Hough, M. Spannuth, M. Nakata, D. A. Coleman, C. D. Jones, G. Dantlgraber, C. Tschierske, J. Watanabe, E. Korblova, D. M. Walba, J. E. Maclennan, M. A. Glaser and N. A. Clark, *Science*, 2009, **325**, 452-456.

116. S. P. Sreenilayam, Y. P. Panarin, J. K. Vij, V. P. Panov, A. Lehmann, M. Poppe, M. Prehm and C. Tschierske, *Nat. Commun.*, 2016, **7**, 11369.

117. L. E. Hough, H. T. Jung, D. Kruerke, M. S. Heberling, M. Nakata, C. D. Jones, D. Chen, D. R. Link, J. Zasadzinski, G. Heppke, J. P. Rabe, W. Stocker, E. Korblova, D. M. Walba, M. A. Glaser and N. A. Clark, *Science*, 2009, **325**, 456-460.

118. D. Chen, J. E. Maclennan, R. Shao, D. K. Yoon, H. T. Wang, E. Korblova, D. M. Walba, M. A. Glaser and N. A. Clark, *J. Am. Chem. Soc.*, 2011, **133**, 12656-12663.

119. H. Kim, S. Lee, T. J. Shin, E. Korblova, D. M. Walba, N. A. Clark, S. B. Lee and D. K. Yoon, *Proc. Natl. Acad. Sci. USA*, 2014, **111**, 14342-14347.

120. H. Kim, S. H. Ryu, M. Tuchband, T. J. Shin, E. Korblova, D. M. Walba, N. A. Clark and D. K. Yoon, *Sci. Adv.*, 2017, **3**, 1602102.

121. W. Lewandowski, N. Vaupotic, D. Pociecha, E. Gorecka and L. M. Liz-Marzan, *Adv. Mater.*, 2020, **32**, 1905591.

122. J. Thisayukta, H. Takezoe and J. Watanabe, *Jpn. J. Appl. Phys. 1*, 2001, **40**, 3277-3287.

123. E. Tsai, J. M. Richardson, E. Korblova, M. Nakata, D. Chen, Y. Q. Shen, R. F. Shao, N. A. Clark and D. M. Walba, *Angew. Chem. Int. Edit.*, 2013, **52**, 5254-5257.

124. S. Shadpour, A. Nemati, M. Salamonczyk, M. E. Prévôt, J. Liu, N. J. Boyd, M. R. Wilson, C. H. Zhu, E. Hegmann, A. I. Jákli and T. Hegmann, *Small*, 2020, **16**, 1905591

125. S. Shadpour, A. Nemati, J. Liu and T. Hegmann, *ACS Appl. Mater. Interf.*, 2020, **12**, 13456-13463.

126. L. Li, M. Salamonczyk, S. Shadpour, C. H. Zhu, A. Jákli and T. Hegmann, *Nat. Commun.*, 2018, **9**, 714.

127. L. Li, M. Salamonczyk, A. Jakli and T. Hegmann, *Small*, 2016, **12**, 3944-3955.

128. M. Alaasar, M. Prehm and C. Tschierske, *Chem.-Eur. J.*, 2016, **22**, 6583-6597.

129. S. Shadpour, A. Nemati, N. J. Boyd, L. Li, M. E. Prévôt, S. L. Wakerlin, J. P. Vanegas, M. Salamonczyk, E. Hegmann, C. H. Zhu, M. R. Wilson, A. I. Jakli and T. Hegmann, *Mater. Horiz.*, 2019, **6**, 959-968.

130. N. A. Hawbaker and D. G. Blackmond, *Nat. Chem.*, 2019, **11**, 957-962.

131. C. Zhang, N. Diorio, O. D. Lavrentovich and A. Jakli, *Nat. Commun.*, 2014, **5**, 3302.

132. G. Pelzl, S. Diele and W. Weissflog, *Adv. Mater.*, 1999, **11**, 707-724.

133. D. M. Walba, L. Eshdat, E. Korblova and R. K. Shoemaker, *Cryst. Growth Des.*, 2005, **5**, 2091-2099.

134. T. Niori, T. Sekine, J. Watanabe, T. Furukawa and H. Takezoe, *J. Mater. Chem.*, 1996, **6**, 1231-1233.

135. J. Matraszek, N. Topnani, N. Vaupotic, H. Takezoe, J. Mieczkowski, D. Pociecha and E. Gorecka, *Angew. Chem. Int. Edit.*, 2016, **55**, 3468-3472.

136. A. Zep, K. Sitkowska, D. Pociecha and E. Gorecka, *J. Mater. Chem. C*, 2014, **2**, 2323-2327.

137. M. Nagaraj, *Liq. Cryst. Today*, 2018, **27**, 41-41.

138. J. W. Goodby, A. J. Slaney, C. J. Booth, I. Nishiyama, J. D. Vuijk, P. Styring and K. J. Toyne, *Mol. Cryst. Liq. Cryst.*, 1994, **243**, 231-298.

139. A. Taugerbeck and C. J. Booth, in *Handbook of Liquid Crystals*, Eds. J. W. Goodby, P. J. Collings, T. Kato, C. Tschierske, H. F. Gleeson and P. Raynes, vol. 3, pp. 1-63, Wiley-VCH, Weinheim.

140. J. Liu, S. Shadpour, M. E. Prévôt, M. Chirgwin, A. Nemati, E. Hegmann, R. P. Lemieux and T. Hegmann, *ACS Nano*, 2021, **15**, 7249-7270.

141. B. Sezgin, J. Liu, N. G. DP, C. Zhu, T. Tilki, M. E. Prévôt and T. Hegmann, *ACS Nanosci. Au*, 2023, **3**, 295-309.

142. H. Niwano, M. Nakata, J. Thisayukta, D. R. Link, H. Takezoe and J. Watanabe, *J. Phys. Chem. B*, 2004, **108**, 14889-14896.

143. W. Park, T. Ha, T. T. Kim, A. Zep, H. Ahn, T. J. Shin, K. I. Sim, T. S. Jung, J. H. Kim, D. Pociecha, E. Gorecka and D. K. Yoon, *NPG Asia Mater.*, 2019, **11**, 45.

144. C. Zhang, G. Fu, Y. Zhu, R. Fu and G. Zhang, *Optik*, 1990, **84**, 119-122.
145. J. Liu, S. Shadpour, A. Nemati, M. E. Prévôt, E. Hegmann, C. H. Zhu and T. Hegmann, *Liq. Cryst.*, 2021, **48**, 1129-1139.
146. J. J. Cheng, G. Le Saux, J. Gao, T. Buffeteau, Y. Battie, P. Barois, V. Ponsinet, M. H. Delville, O. Ersen, E. Pouget and R. Oda, *ACS Nano*, 2017, **11**, 3806-3818.
147. A. Kuzyk, R. Schreiber, Z. Y. Fan, G. Pardatscher, E. M. Roller, A. Hogele, F. C. Simmel, A. O. Govorov and T. Liedl, *Nature*, 2012, **483**, 311-314.
148. S. H. Ren, R. Prakash, D. Wang, V. S. K. Chakravadhanula and M. Fichtner, *ChemSusChem*, 2012, **5**, 1397-1400.
149. G. Z. Hu, F. Nitze, H. R. Barzegar, T. Sharifi, A. Mikolajczuk, C. W. Tai, A. Borodzinski and T. Wagberg, *J. Power Sources*, 2012, **209**, 236-242.
150. G. Z. Hu, F. Nitze, T. Sharifi, H. R. Barzegar and T. Wagberg, *J. Mater. Chem.*, 2012, **22**, 8541-8548.
151. X. Q. Chen, S. L. Zhang, D. A. Dikin, W. Q. Ding, R. S. Ruoff, L. J. Pan and Y. Nakayama, *Nano Lett.*, 2003, **3**, 1299-1304.
152. R. R. Naik, S. J. Stringer, G. Agarwal, S. E. Jones and M. O. Stone, *Nat. Mater.*, 2002, **1**, 169-172.
153. J. M. Slocik, M. O. Stone and R. R. Naik, *Small*, 2005, **1**, 1048-1052.
154. A. D. Merg, J. C. Boatz, A. Mandal, G. P. Zhao, S. Mokashi-Punekar, C. Liu, X. T. Wang, P. J. Zhang, P. C. A. van der Wel and N. L. Rosi, *J. Am. Chem. Soc.*, 2016, **138**, 13655-13663.
155. C. L. Chen, P. J. Zhang and N. L. Rosi, *J. Am. Chem. Soc.*, 2008, **130**, 13555-13557.
156. C. L. Chen and N. L. Rosi, *Angew. Chem. Int. Edit.*, 2010, **49**, 1924-1942.
157. S. Xu, Y. F. Wang, W. Qi, R. X. Su and Z. M. He, *Chemistryselect*, 2018, **3**, 4939-4943.
158. M. Baginski, M. Tupikowska, G. Gonzalez-Rubio, M. Wojcik and W. Lewandowski, *Adv. Mater.*, 2020, **32**, 1904581.
159. D. Grzelak, M. Tupikowska, D. Vila-Liarte, D. Beutel, M. Baginski, S. Parzyszek, M. Gora, C. Rockstuhl, L. M. Liz-Marzan and W. Lewandowski, *Adv. Funct. Mater.*, 2022, **32**, 2111280.
160. M. Pawlak, M. Baginski, P. Llombart, D. Beutel, G. Gonzalez-Rubio, E. Gorecka, C. Rockstuhl, J. Mieczkowski, D. Pociecha and W. Lewandowski, *Chem. Commun.*, 2022, **58**, 7364-7367.
161. V. M. Marx, H. Girgis, P. A. Heiney and T. Hegmann, *J. Mater. Chem.*, 2008, **18**, 2983-2994.
162. J. Mirzaei, M. Urbanski, H. S. Kitzerow and T. Hegmann, *ChemPhysChem*, 2014, **15**, 1381-1394.
163. D. P. N. Gonçalves and T. Hegmann, *Angew. Chem. Int. Edit.*, 2021, **60**, 17344-17349.
164. B. Sezgin and T. Hegmann, *J. Mater. Chem. C*, 2022, **10**, 18120-18126.
165. D. Chen, C. H. Zhu, H. T. Wang, J. E. Maclennan, M. A. Glaser, E. Korblova, D. M. Walba, J. A. Rego, E. A. Soto-Bustamante and N. A. Clark, *Soft Matter*, 2013, **9**, 462-471.
166. R. A. Callahan, D. C. Coffey, D. Chen, N. A. Clark, G. Rumbles and D. M. Walba, *ACS Appl. Mater. Interf.*, 2014, **6**, 4823-4830.
167. W. Park, J. M. Wolska, D. Pociecha, E. Gorecka and D. K. Yoon, *Adv. Opt. Mater.*, 2019, **7**, 1901399.
168. G. Park, H. Park, J. M. Wolska, J. G. Park and D. K. Yoon, *Mater. Horiz.*, 2022, **9**, 2542-2550.
169. U. Tohgha, K. K. Deol, A. G. Porter, S. G. Bartko, J. K. Choi, B. M. Leonard, K. Varga, J. Kubelka, G. Muller and M. Balaz, *ACS Nano*, 2013, **7**, 11094-11102.
170. J. T. Lin, D. G. Chen, L. S. Yang, T. C. Lin, Y. H. Liu, Y. C. Chao, P. T. Chou and C. W. Chiu, *Angew. Chem. Int. Edit.*, 2021, **60**, 21434-21440.
171. H. Tanaka, Y. Inoue and T. Mori, *ChemPhotoChem*, 2018, **2**, 386-402.
172. H. Anetai, T. Takeda, N. Hoshino, Y. Arak, T. Wada, S. Yamamoto, M. Mitsuishi, H. Tsuchida, T. Ogoshi and T. Akutagawa, *J. Phys. Chem. C*, 2018, **122**, 6323-6331.
173. Y. Y. Dang, X. L. Liu, Y. J. Sun, J. W. Song, W. P. Hu and X. T. Tao, *J. Phys. Chem. Lett.*, 2020, **11**, 1689-1696.
174. Y. B. Tan, Y. Okayasu, S. Katao, Y. Nishikawa, F. Asanoma, M. Yamada, J. Yuasa and T. Kawai, *J. Am. Chem. Soc.*, 2020, **142**, 17653-17661.
175. S. Xue, L. M. Meng, R. S. Wen, L. Shi, J. W. Lam, Z. Y. Tang, B. S. Li and B. Z. Tang, *RSC Adv.*, 2017, **7**, 24841-24847.
176. Y. T. Sang, J. L. Han, T. H. Zhao, P. F. Duan and M. H. Liu, *Adv. Mater.*, 2020, **32**, 1900110.
177. J. Kumar, T. Nakashima and T. Kawai, *J. Phys. Chem. Lett.*, 2015, **6**, 3445-3452.
178. H. K. Li, J. Cheng, Y. H. Zhao, J. W. Y. Lam, K. S. Wong, H. K. Wu, B. S. Li and B. Z. Tang, *Mater. Horiz.*, 2014, **1**, 518-521.
179. J. F. Li, C. X. Hou, C. Huang, S. Q. Xu, X. L. Peng, Q. Qi, W. Y. Lai and W. Huang, *Research-China*, 2020, **2020**, 3839160.
180. J. Z. Liu, H. M. Su, L. M. Meng, Y. H. Zhao, C. M. Deng, J. C. Y. Ng, P. Lu, M. Faisal, J. W. Y. Lam, X. H. Huang, H. K. Wu, K. S. Wong and B. Z. Tang, *Chem. Sci.*, 2012, **3**, 2737-2747.
181. Z. W. Luo, L. Tao, C. L. Zhong, Z. X. Li, K. Lan, Y. Feng, P. Wang and H. L. Xie, *Macromolecules*, 2020, **53**, 9758-9768.
182. K. Ma, W. J. Chen, T. F. Jiao, X. Jin, Y. T. Sang, D. Yang, J. Zhou, M. H. Liu and P. F. Duan, *Chem. Sci.*, 2019, **10**, 6821-6827.
183. X. J. Li, W. R. Hu, Y. X. Wang, Y. W. Quan and Y. X. Cheng, *Chem. Commun.*, 2019, **55**, 5179-5182.
184. X. J. Li, Q. Li, Y. X. Wang, Y. W. Quan, D. Z. Chen and Y. X. Cheng, *Chem.-Eur. J.*, 2018, **24**, 12607-12612.
185. J. D. Luo, Z. L. Xie, J. W. Y. Lam, L. Cheng, H. Y. Chen, C. F. Qiu, H. S. Kwok, X. W. Zhan, Y. Q. Liu, D. B. Zhu and B. Z. Tang, *Chem. Commun.*, 2001, 1740-1741.
186. J. Liu, Y. Molard, M. E. Prévôt and T. Hegmann, *ACS Appl. Mater. Interf.*, 2022, **14**, 29398-29411.
187. S. Parzyszek, J. Tessarolo, A. Pedrazo-Tardaos, A. M. Ortuno, M. Baginski, S. Bals, G. H. Clever and W. Lewandowski, *ACS Nano*, 2022, **16**, 18472-18482.
188. M. W. C. C. Greenshields, I. A. Hummelgen, M. A. Mamo, A. Shaikjee, S. D. Mhlanga, W. A. L. van Otterlo and N. J. Coville, *J. Nanosci. Nanotechnol.*, 2011, **11**, 10211-10218.
189. Y. Gao, F. Y. Guo, P. Cao, J. C. Liu, D. M. Li, J. Wu, N. Wang, Y. W. Su and Y. Zhao, *ACS Nano*, 2020, **14**, 3442-3450.
190. S. Y. Shi, Y. G. He, W. W. Chen, N. Liu, Y. Y. Zhu, Y. S. Ding, J. Yin and Z. Q. Wu, *Macromol. Rapid Comm.*, 2015, **36**, 1511-1520.
191. Y. M. Wang, W. Li, T. T. Liu, L. Xu, Y. Y. Guo, J. Ke, S. M. Li and H. R. Li, *Mat. Sci. Eng. C*, 2019, **103**, 109826.
192. R. S. Li, J. H. Liu, H. Shi, P. P. Hu, Y. Wang, P. F. Gao, J. Wang, M. Y. Jia, H. W. Li, Y. F. Li, C. D. Mao, N. Li and C. Z. Huang, *Nano Lett.*, 2021, **21**, 8455-8465.
193. Y. Wang, J. Xu, Y. W. Wang and H. Y. Chen, *Chem. Soc. Rev.*, 2013, **42**, 2930-2962.

194. D. Vila-Liarte, N. A. Kotov and L. M. Liz-Marzán, *Chem. Sci.*, 2022, **13**, 595-610.
195. N. A. Kotov, L. M. Liz-Marzán and P. S. Weiss, *ACS Nano*, 2021, **15**, 12457-12460.
196. W. B. Wu and M. Pauly, *Mater. Adv.*, 2022, **3**, 186-215.
197. W. Ma, L. G. Xu, A. F. de Moura, X. L. Wu, H. Kuang, C. L. Xu and N. A. Kotov, *Chem. Rev.*, 2017, **117**, 8041-8093.
198. L. L. Tan, S. J. Yu, Y. R. Jin, J. M. Li and P. P. Wang, *Angew. Chem. Int. Edit.*, 2022, **61**, e202112400.
199. M. Kim, M. O. Bazaid, H. J. Lee, S. S. Jang, Y. J. Jang and D. H. Kim, *Chem. Mater.*, 2023, **35**, 3073-3082.
200. Y. F. Wang, W. Qi, R. L. Huang, X. J. Yang, M. F. Wang, R. X. Su and Z. M. He, *J. Am. Chem. Soc.*, 2015, **137**, 7869-7880.
201. Y. Shen and C. F. Chen, *Chem. Rev.*, 2012, **112**, 1463-1535.
202. M. Gingras, *Chem. Soc. Rev.*, 2013, **42**, 968-1006.
203. M. Gingras, G. Felix and R. Peresutti, *Chem. Soc. Rev.*, 2013, **42**, 1007-1050.
204. M. Gingras, *Chem. Soc. Rev.*, 2013, **42**, 1051-1095.
205. N. Chouaieb, A. Goriely and J. H. Maddocks, *Proc. Natl. Acad. Sci. USA*, 2006, **103**, 9398-9403.
206. A. Nemati, S. Shadpour, L. Querciagrossa, L. Li, T. Mori, M. Gao, C. Zannoni and T. Hegmann, *Nat. Commun.*, 2018, **9**, 3908.
207. A. Nemati, L. Querciagrossa, C. Callison, S. Shadpour, D. P. N. Gonçalves, T. Mori, X. M. Cui, R. Q. Ai, J. F. Wang, C. Zannoni and T. Hegmann, *Sci. Adv.*, 2022, **8**, eabl4385.
208. D. P. N. Gonçalves, T. Hegmann and T. Ogolla, *ChemPhysChem*, 2023, **24**, e202200685.
209. X. Zhu, P. Duan, L. Zhang and M. Liu, *Chem.-Eur. J.*, 2011, **17**, 3429-3437.
210. M. Liu, L. Zhang and T. Wang, *Chem. Rev.*, 2015, **115**, 7304-7397.
211. L. Zhang, T. Wang, Z. Shen and M. Liu, *Adv. Mater.*, 2016, **28**, 1044-1059.
212. H. Jiang, Y. Jiang, J. Han, L. Zhang and M. Liu, *Angew. Chem. Int. Ed.*, 2019, **58**, 785-790.
213. T. Shimizu, M. Masuda and H. Minamikawa, *Chem. Rev.*, 2005, **105**, 1401-1443.
214. D. N. Nadimetla, M. Al Kobaisi, S. T. Budge and S. V. Bhosale, *Chem. Rec.*, 2020, **20**, 793-819.
215. T. Aida and E. W, Meijer, *Isr. J. Chem.*, 2020, **60**, 33-47.
216. J. V. Selinger, M. S. Spector and J. M. Schnur, *J. Phys. Chem. B*, 2001, **105**, 7157-7169.
217. H. Takezoe, H., in C. Tschierske (Ed.) *Liquid Crystals. Topics in Current Chemistry*, vol. **318**, 303-330, Springer, Berlin, Heidelberg (2011).
218. C. Tschierske and G. Ungar, *ChemPhysChem*, 2016, **17**, 9-26.
219. K. V. Le, H. Takezoe and F. Araoka, *Adv. Mater.*, 2017, **29**, 1602737.
220. C. Tschierske, *Liq. Cryst.*, 2018, **45**, 2221-2252.

TOC Entry

Chiral filamentous structures are omnipresent in nature and our daily life. This review provides an overview over the main types of nano- and microfilaments, delineates the modes of formation based on the concept of intra- or interlayer misfits, and gives example applications largely based on their ability to serve as templates.

Group Photograph Accompanying Text

The interdisciplinary research team, including chemists, physicists, and engineers, led by Prof. Torsten Hegmann (Ph.D., Martin Luther University Halle-Wittenberg, Halle (Germany), Fellow of the Royal Society of Chemistry, Ohio Research Scholar, and currently serving as the Director of the Advanced Materials and Liquid Crystal Institute at Kent State University) focuses on research that explores the interface and interactions between lyotropic and thermotropic liquid crystals and a wide range of nanomaterials, the self-assembly in soft matter, nanomaterial chirality generation, visualization, transfer, and amplification, chiral organic nano- and microfilaments and their use as templates, as well as liquid crystal toxic gas and vapor sensors. In the photograph that shows all coauthors (taken in the Spring of 2023) from left-to-right; front row: Grace A. R. Rohaley (Ph.D. student), Dr. Marianne E. Prévôt (Ph.D., University of Rennes), Andrea Oprandi (Ph.D. student); back row: Gourab Acharjee (Ph.D. student), Dr. Suraj Kumar Pathak (Ph.D., Indian Institute of Technology, Guwahati (India)), Dr. Ashwathanarayana Gowda (Ph.D., C. V. Raman Research Institute, Bengaluru (India)), Prof. Torsten Hegmann, Dr. Barış Sezgin (Ph.D., Süleyman Demirel University, Isparta (Turkey); contributed to work highlighted in this review, but not the writing of this review itself), and Ryan Williams (Ph.D. student).

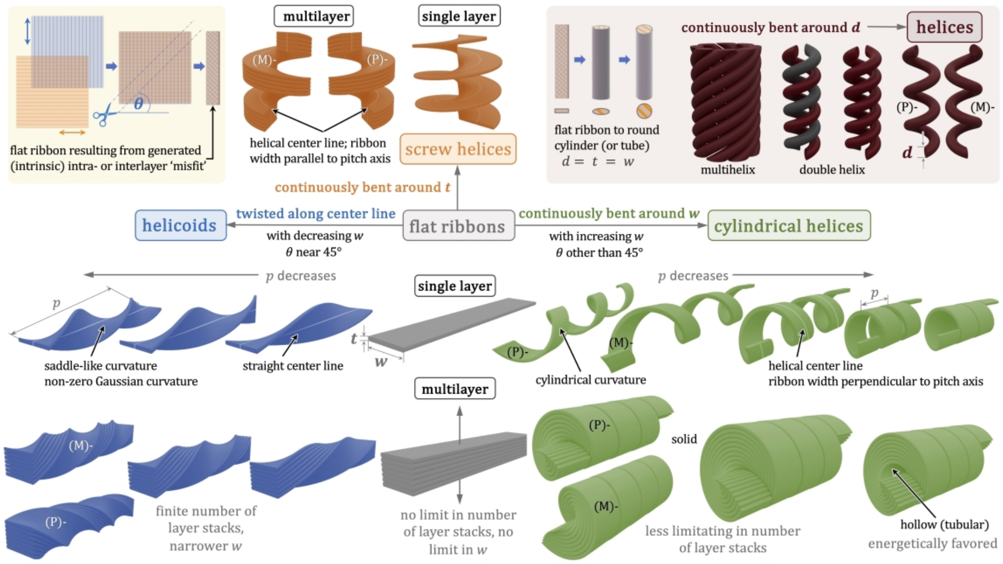

given in main manuscript

2266x1275mm (72 x 72 DPI)

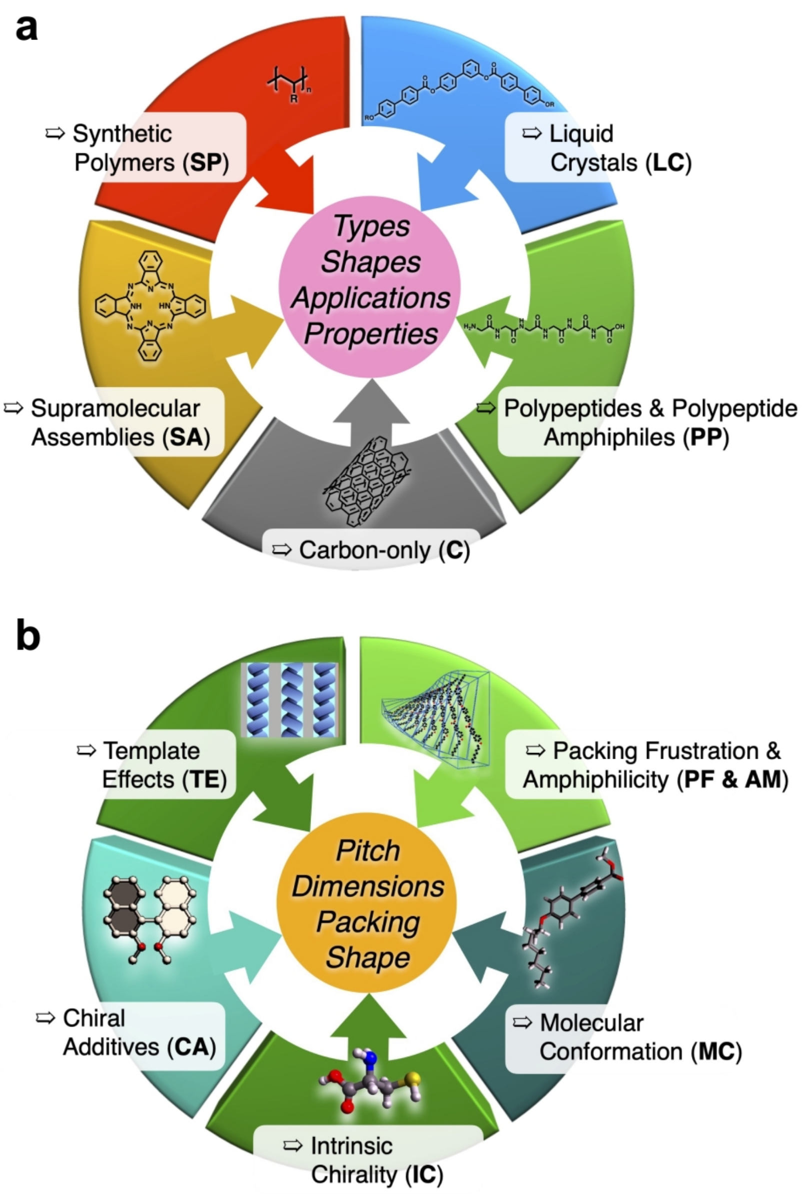

given in main manuscript

940x1376mm (72 x 72 DPI)

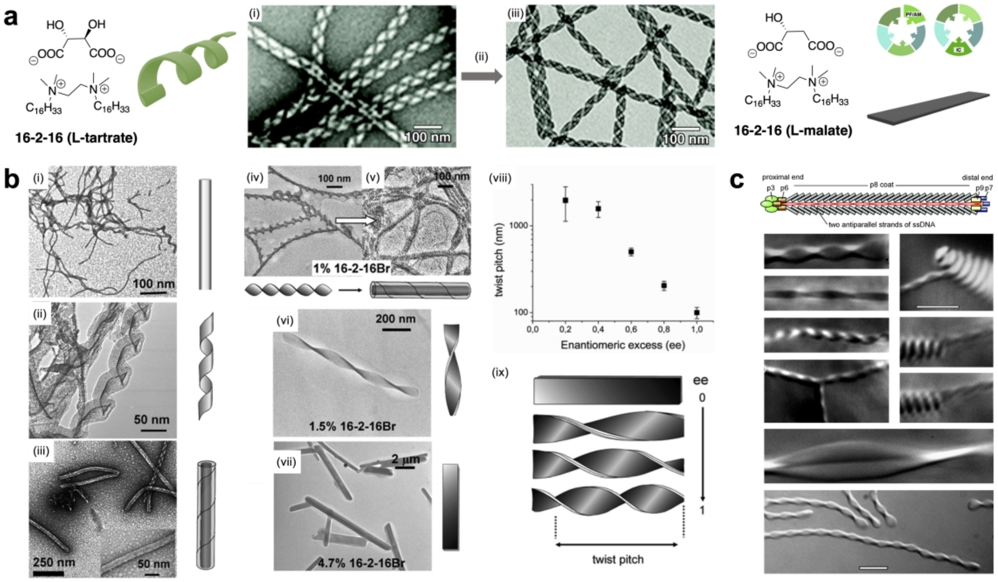

given in main manuscript

2027x1179mm (72 x 72 DPI)

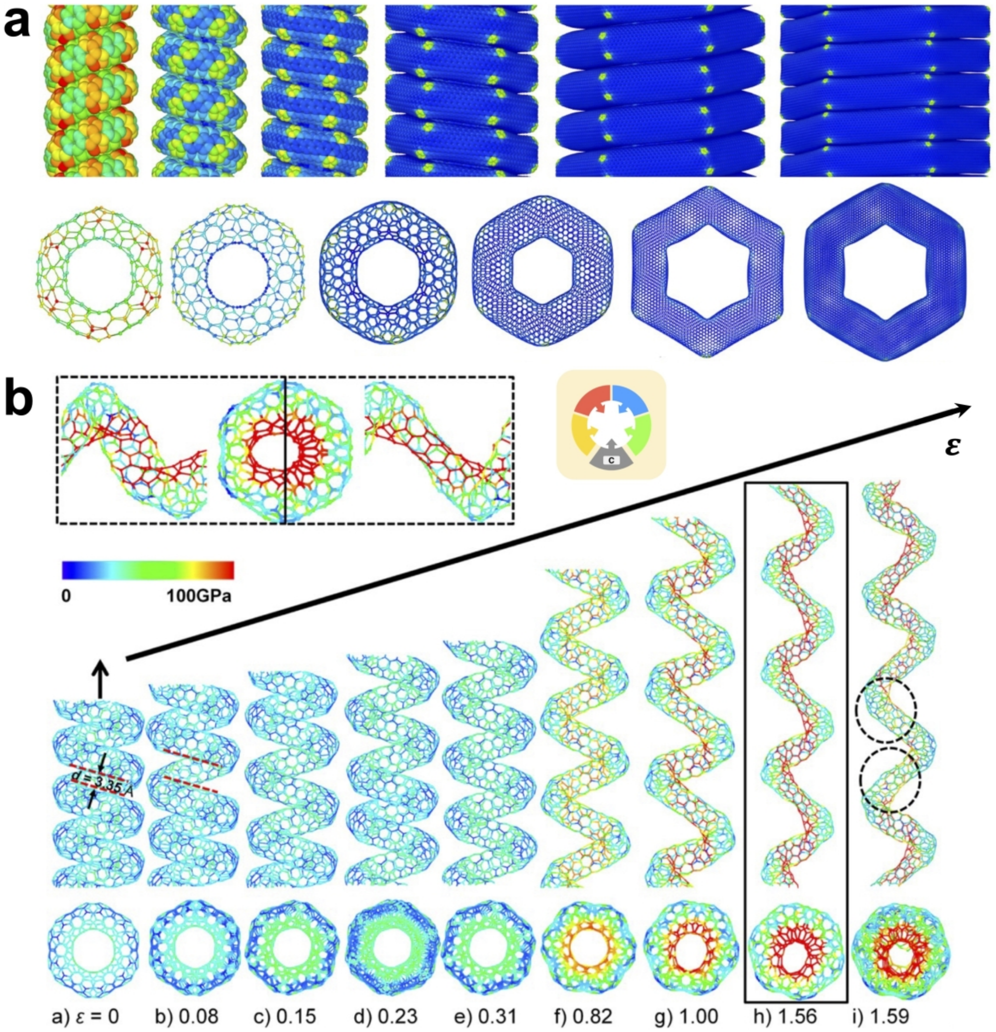

given in main manuscript

1243x1279mm (72 x 72 DPI)

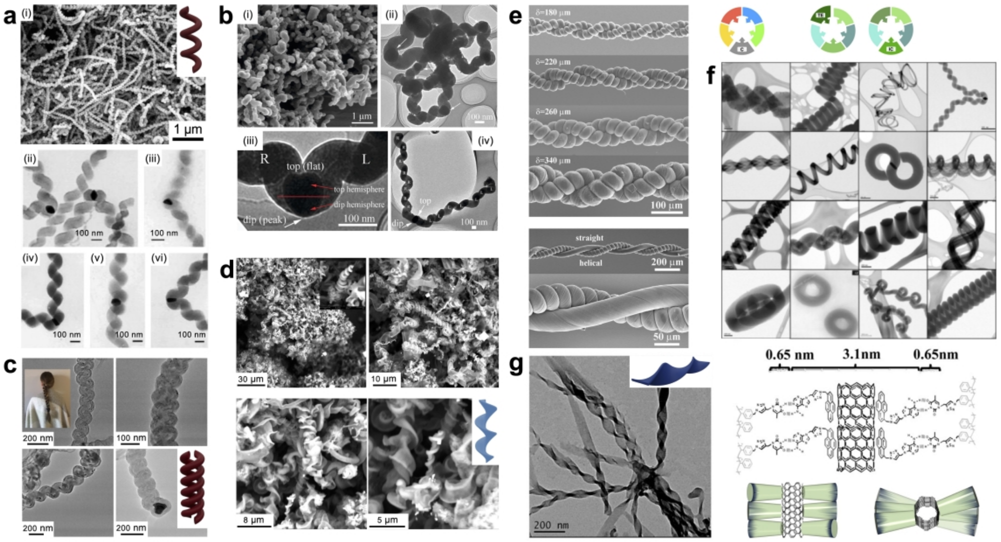

given in main manuscript

2214x1190mm (72 x 72 DPI)

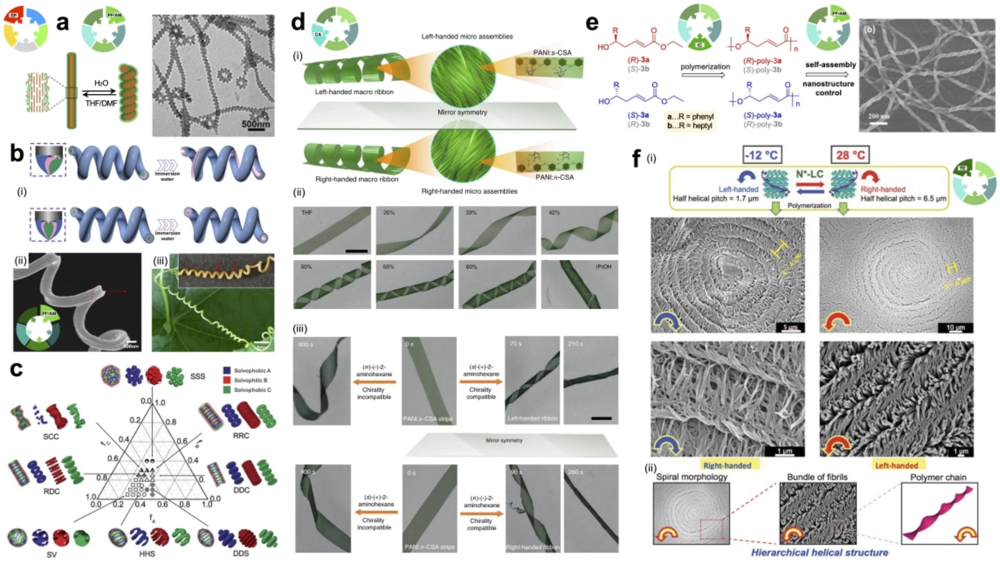

given in main manuscript

2261x1261mm (72 x 72 DPI)

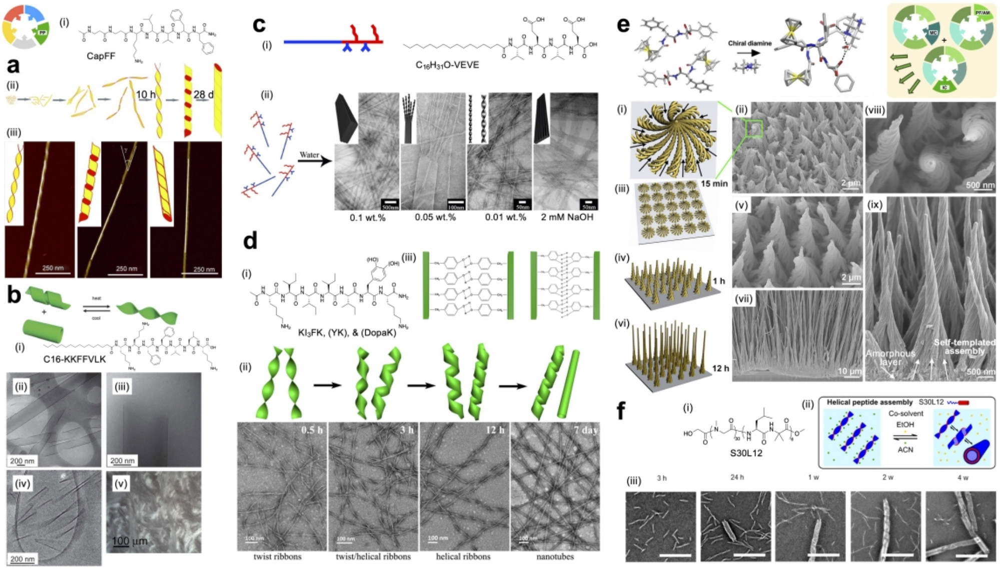

given in main manuscript

2249x1277mm (72 x 72 DPI)

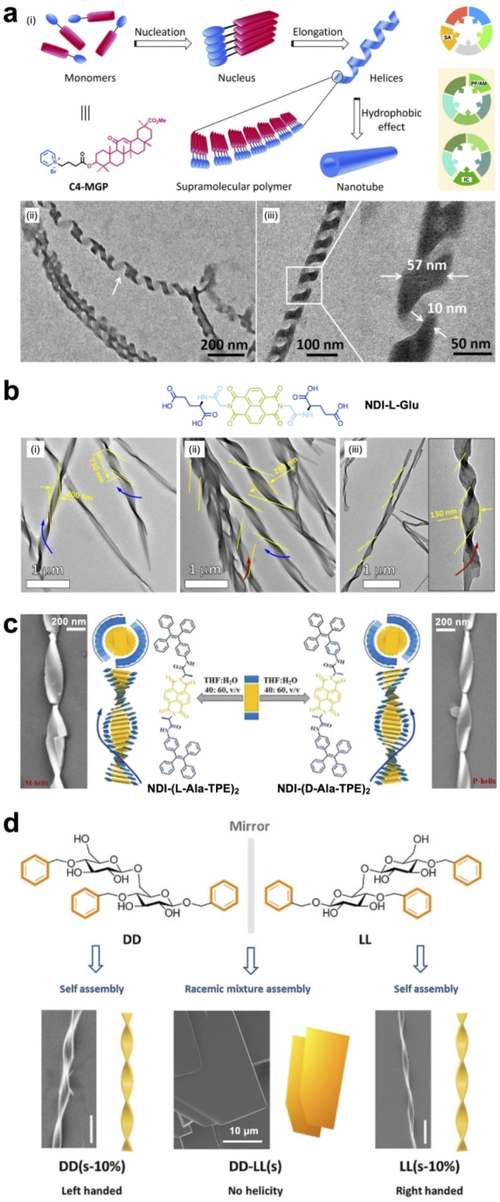

given in main manuscript

904x2153mm (72 x 72 DPI)

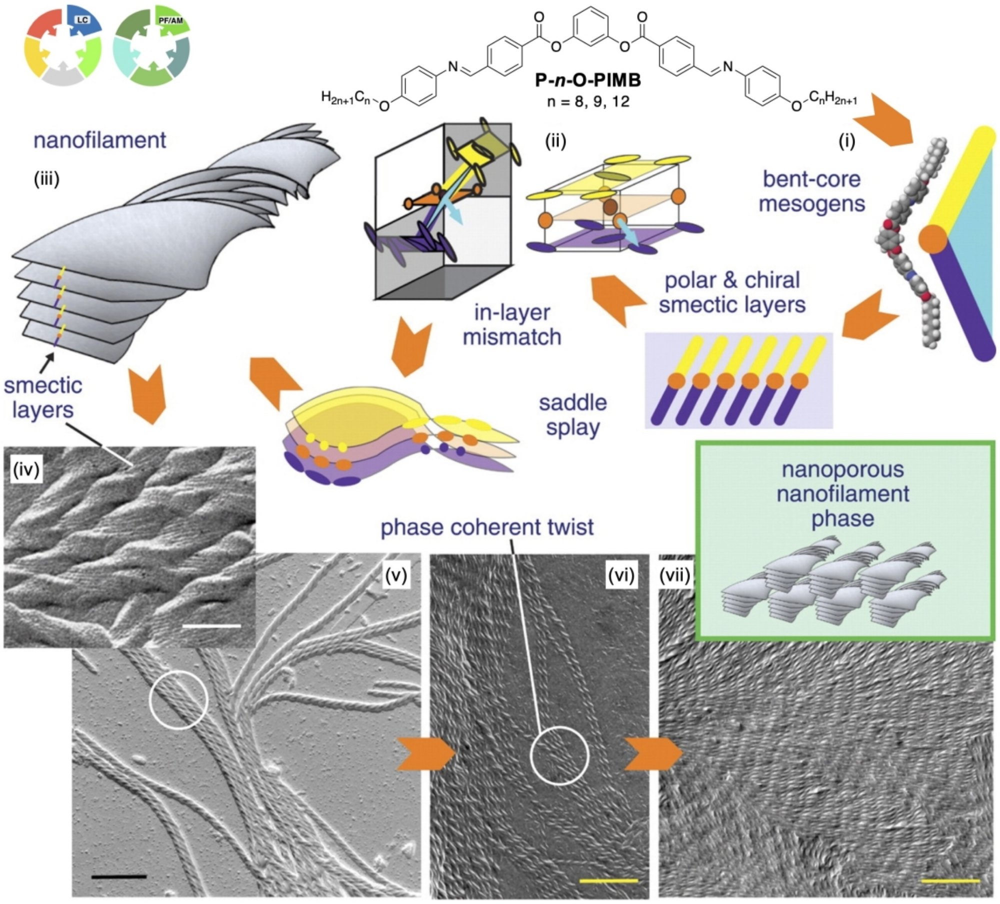

given in main manuscript

950x856mm (72 x 72 DPI)

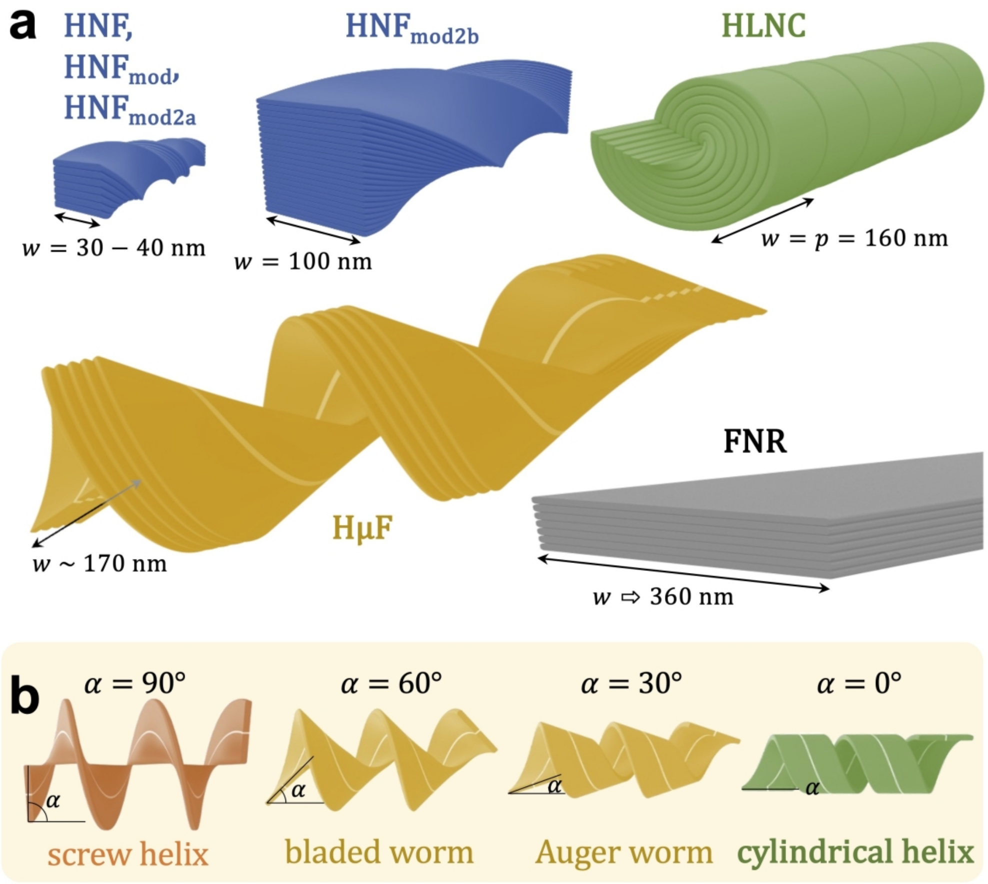

given in main manuscript

938x850mm (72 x 72 DPI)

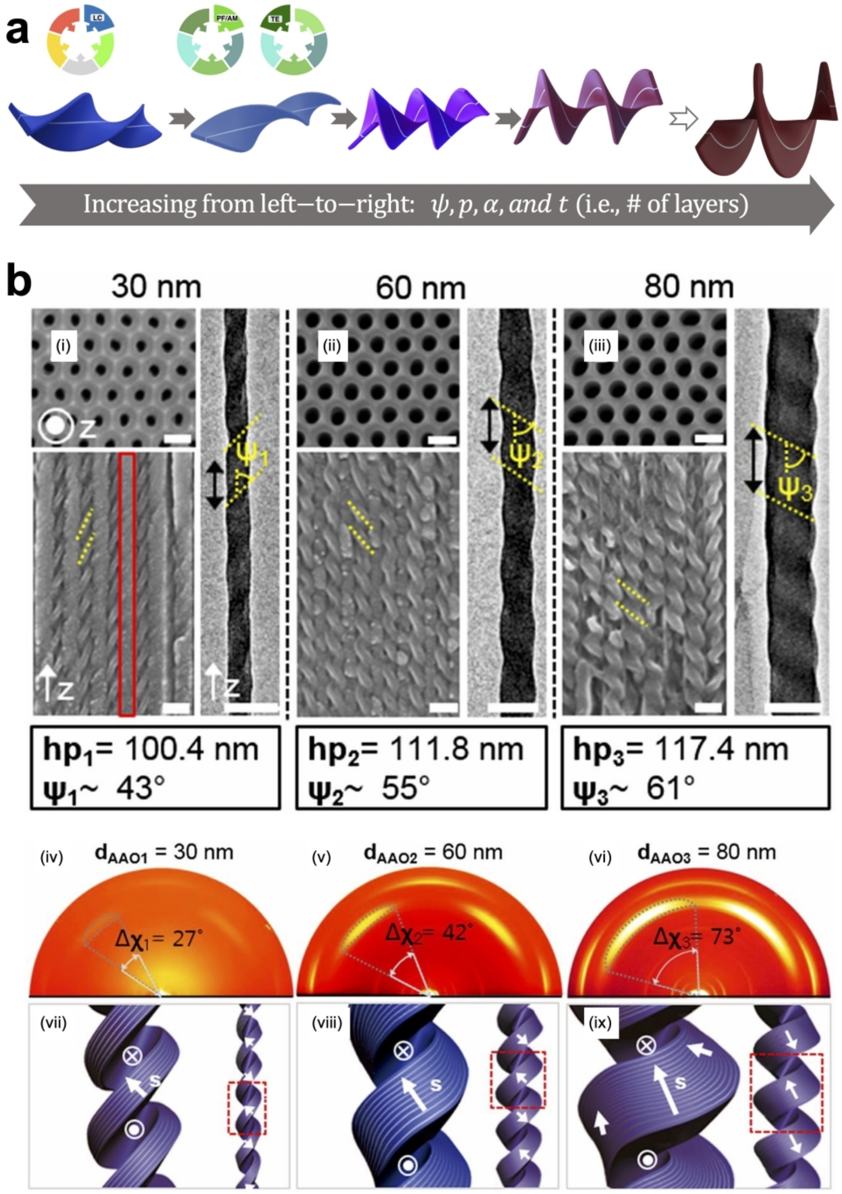

given in main manuscript

923x1314mm (72 x 72 DPI)

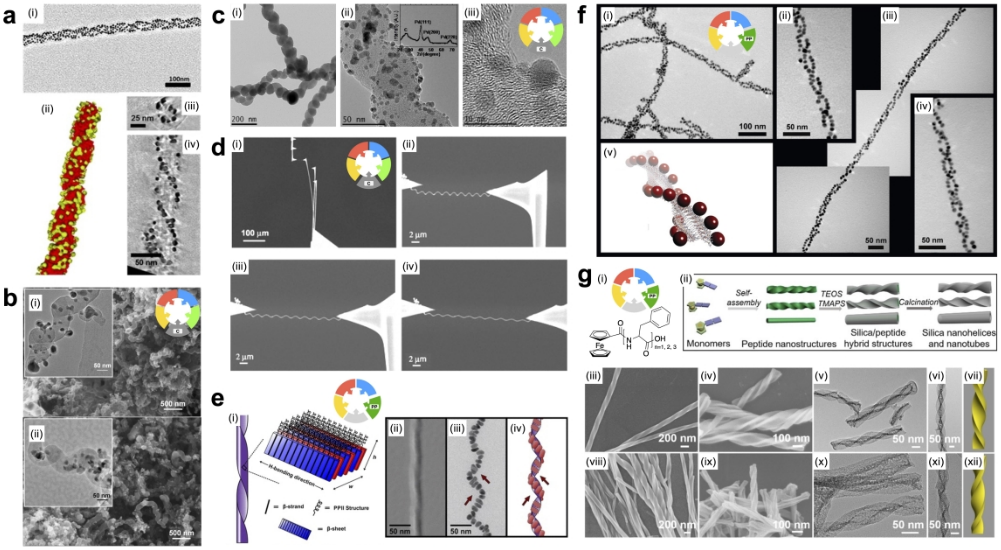

given in main manuscript

2234x1228mm (72 x 72 DPI)

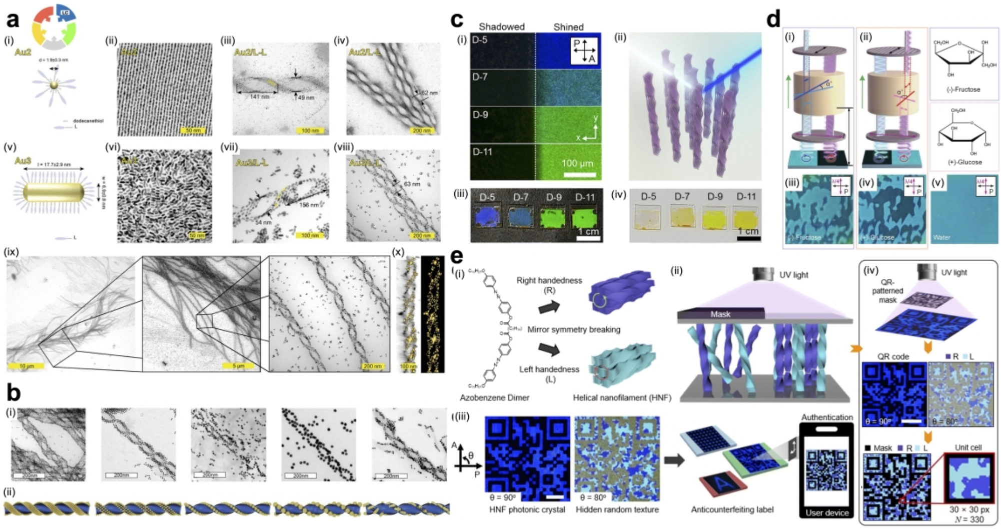

given in main manuscript

2258x1190mm (72 x 72 DPI)

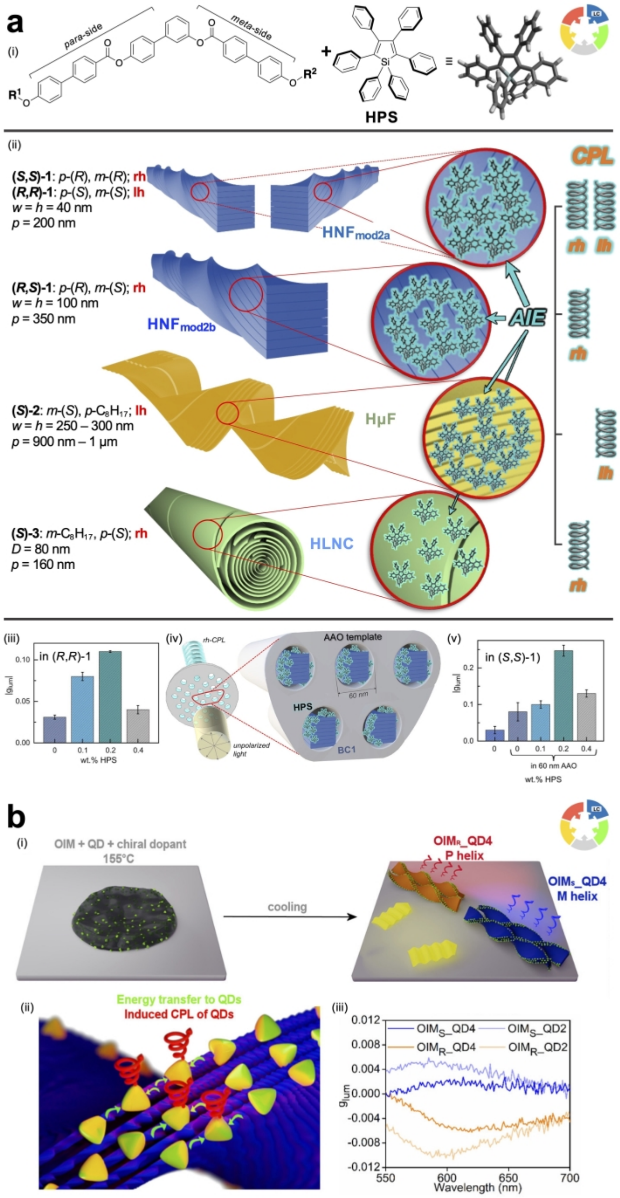

given in main manuscript

947x1826mm (72 x 72 DPI)

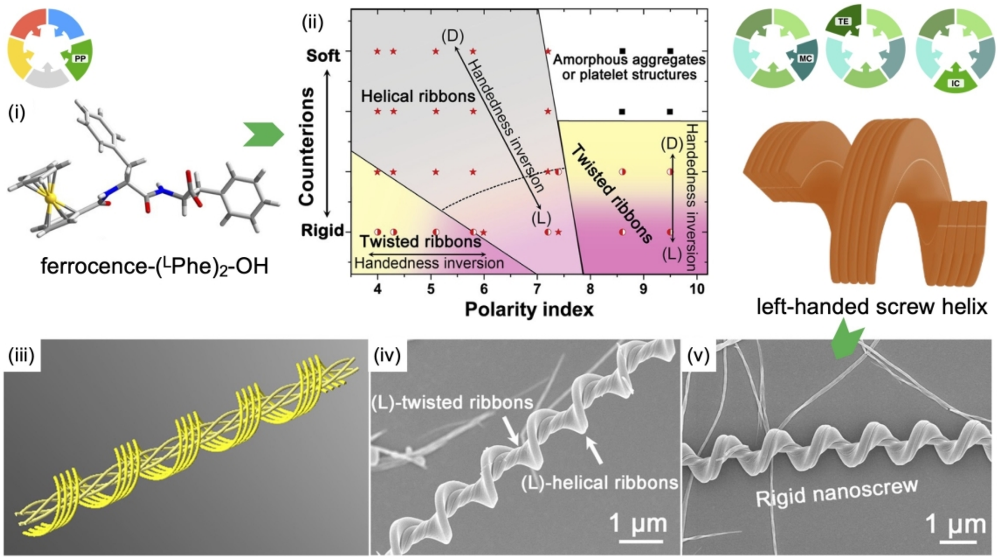

given in main manuscript

922x525mm (72 x 72 DPI)

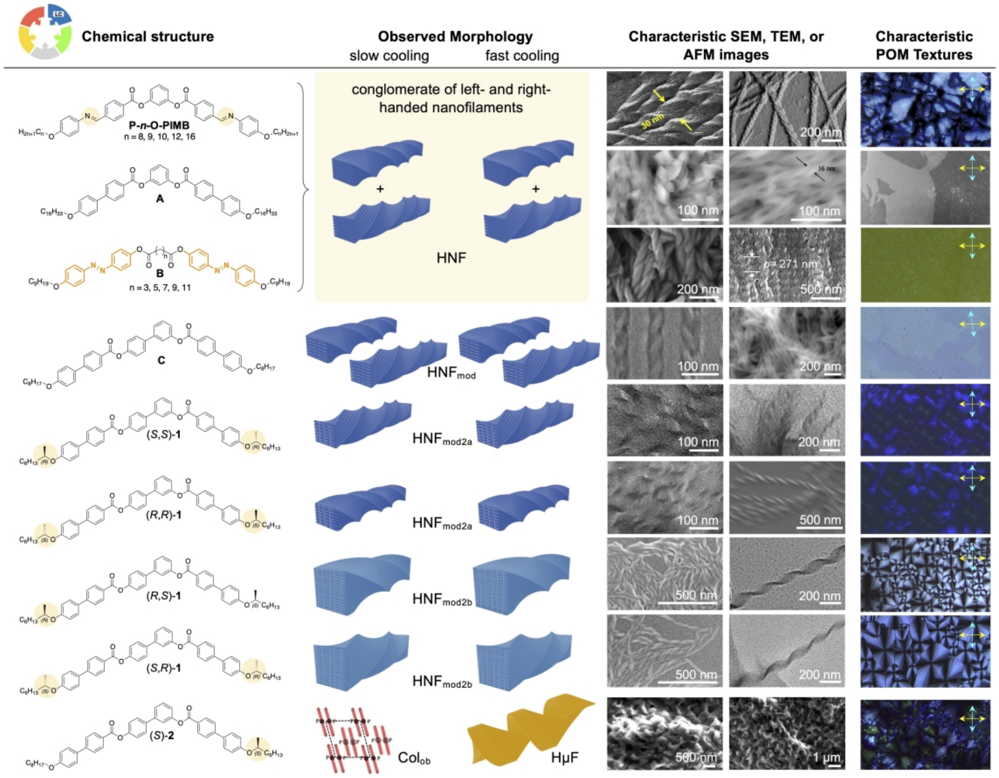

given in main manuscript

1629x1268mm (72 x 72 DPI)

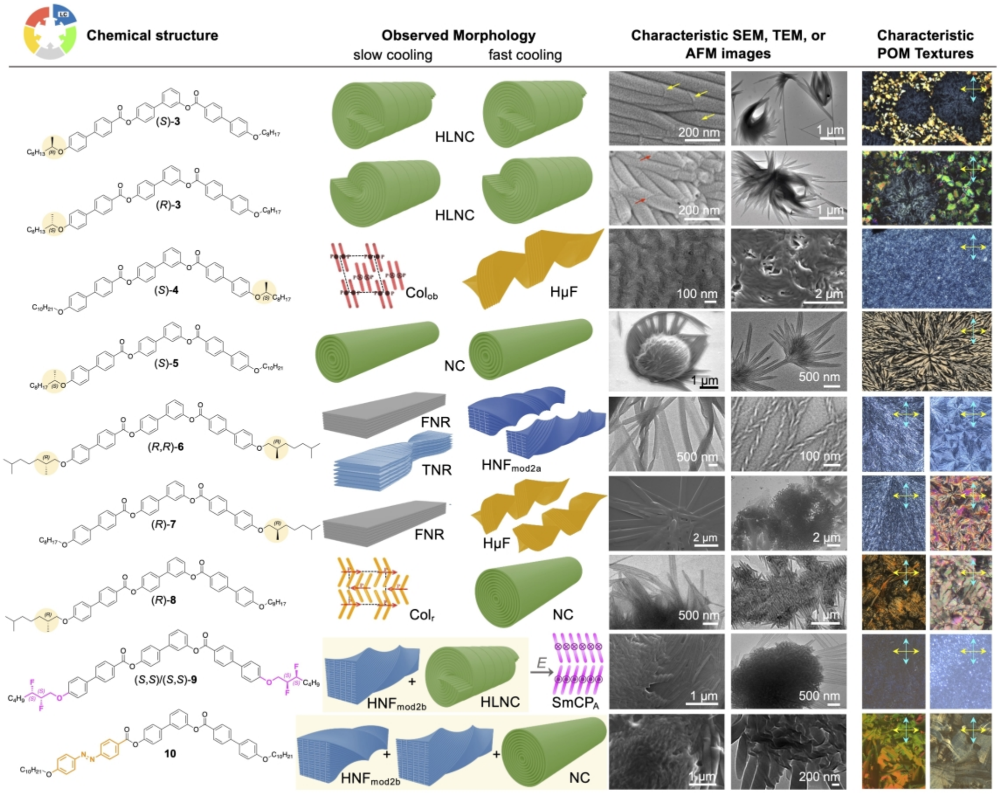

given in main manuscript

1636x1298mm (72 x 72 DPI)